AD-A115 210 AERODYNE RESEARCH INC BEDFORD MA F/G 4/1
EXCEDE SUPPORT STUDIES.(U)
SEP 81 M S ZAHNISER, W CHENG, F BIEN, R LYONS F19628-80-C-0105
UNCLASSIFIED ARI-RR-269 AFGL-TR-81-0257 NL

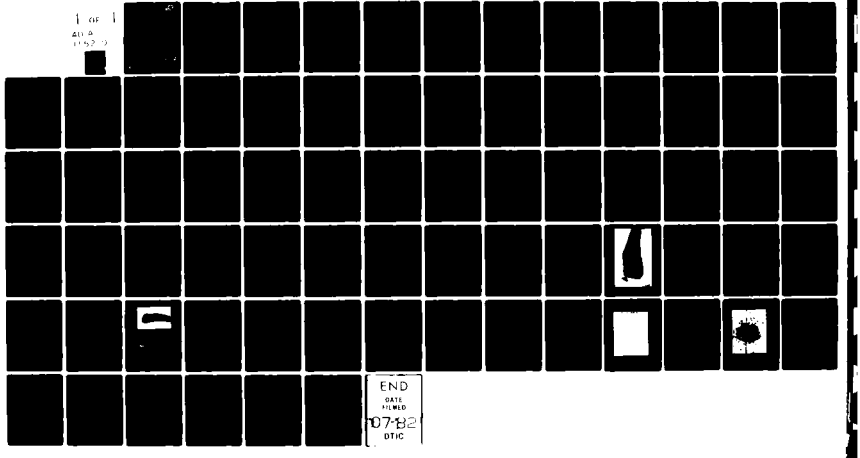

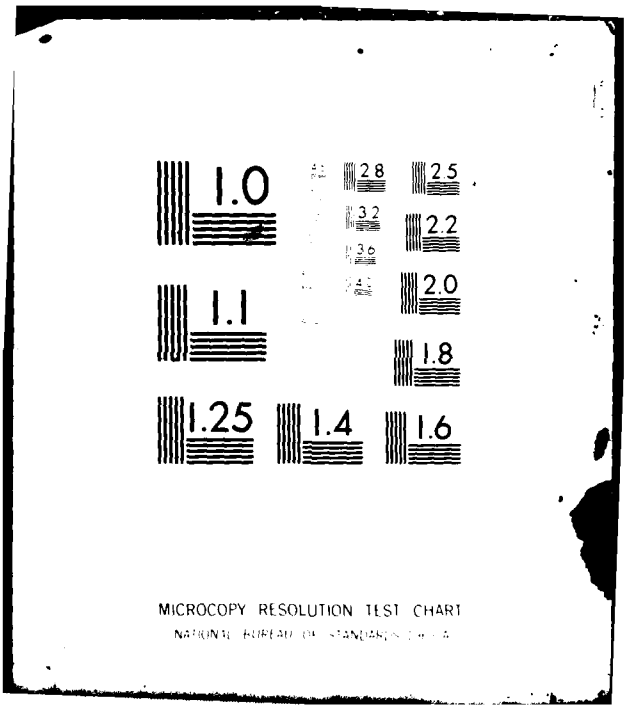
1.0
2.8
2.5
3.2
2.2
3.6
2.0
1.1
1.8
1.25
1.4
1.6
MICROCOPY RESOLUTION TEST CHART

AFGL-TR-81-0257

EXCEDE SUPPORT STUDIES

Mark S. Zahniser
Wai Cheng
Fritz Bien
Robert Lyons

Aerodyne Research, Inc.
Bedford Research Park
Crosby Drive
Bedford, Massachusetts 01730

Final Report
15 May 1980 - 15 September 1981

15 September 1981

AIR FORCE GEOPHYSICS LABORATORY
AIR FORCE SYSTEMS COMMAND
UNITED STATES AIR FORCE
HANSCOM AFB, MASSACHUSETTS 01731

UNCLASSIFIED

SECURITY CLASSIFICATION OF THIS PAGE (When Data Entered)

REPORT DOCUMENTATION PAGE		READ INSTRUCTIONS BEFORE COMPLETING FORM
1. REPORT NUMBER AFGL-TR-81-0257	2. GOVT ACCESSION NO. AD-A115210	3. RECIPIENT'S CATALOG NUMBER
4. TITLE (and Subtitle) EXCEDE SUPPORT STUDIES		5. TYPE OF REPORT & PERIOD COVERED Final Report May 1980 - Sept. 1981
		6. PERFORMING ORG. REPORT NUMBER ARI-RR-269
7. AUTHOR(s) Mark S. Zahniser, Wai Cheng, Fritz Bien, Robert Lyons		8. CONTRACT OR GRANT NUMBER(s) F19628-80-C-0105
9. PERFORMING ORGANIZATION NAME AND ADDRESS Aerodyne Research, Inc. Crosby Drive, Bedford Research Park Bedford, MA 01730		10. PROGRAM ELEMENT, PROJECT, TASK AREA & WORK UNIT NUMBERS 61102F 2310G4AQ
11. CONTROLLING OFFICE NAME AND ADDRESS Air Force Geophysics Laboratory Hanscom AFB, Massachusetts 01731 Monitor/Robert R. O'Neil/OPR		12. REPORT DATE 15 September 1981
		13. NUMBER OF PAGES 72
14. MONITORING AGENCY NAME & ADDRESS(if different from Controlling Office)		15. SECURITY CLASS. (of this report) UNCLASSIFIED
		15a. DECLASSIFICATION/DOWNGRADING SCHEDULE

16. DISTRIBUTION STATEMENT (of this Report)

Approved for public release; distribution unlimited

17. DISTRIBUTION STATEMENT (of the abstract entered in Block 20, if different from Report)

18. SUPPLEMENTARY NOTES

19. KEY WORDS (Continue on reverse side if necessary and identify by block number)

EXCEDE, electron beam, thermosphere, aurora, LWIR, NO^+, air afterglow, hypersonic wake

20. ABSTRACT (Continue on reverse side if necessary and identify by block number)

Various aspects relating to the EXCEDE artificial aurora project are discussed: 1) Data from EXCEDE SPECTRAL in the 4.5 to 5 μm region taken by infrared circular variable filters is analyzed for emission from CO, N_2O, and NO^+. The spectral band profile and altitude dependence of the 4.5 μm feature correlates with a model for NO^+ chemiluminescent emission. 2) A preliminary analysis of spectra in the 12 to 22 μm region shows CO_2 ν_2 radiation at 15 μm to be the predominant feature. Altitude profiles for peaks at 14 and 16 μm

DD FORM 1 JAN 73 1473 EDITION OF 1 NOV 65 IS OBSOLETE
S/N 0102-LF-014-6601

UNCLASSIFIED
SECURITY CLASSIFICATION OF THIS PAGE (When Data Entered)

cont.

are presented. 3) The flowfield for the hypersonic wake of the EXCEDE vehicle at lower altitudes is characterized. Intensity patterns in photographs taken with the on-board visible camera are explained in terms of bow shock and wake shock formation and a procedure is outlined for analyzing the radiometric data in terms of this effect. 4) The long lived electron beam-induced chemiluminescent trail of the Precede I experiment recorded from ground based photography has been analyzed for intensity and altitude distribution. The air afterglow reaction $NO + O \rightarrow NO_2 + h\nu$, from beam-produced NO and ambient atomic oxygen, is not sufficiently strong to account for the observed 10 k Rayleigh intensity.

TABLE OF CONTENTS

INTRODUCTION

This report analyzes spectral and photographic data for various aspects of the EXCEDE program: infrared circular variable filter spectra in the 4.5 to 5 μm region and in the 12 to 22 μm region are analyzed to determine the emitting species produced by the electron beam; intensity patterns in photographs taken with the on-board camera in the EXCEDE: Spectral experiment are used to explain the nature of the hypersonic flow patterns which result in shock waves behind the vehicle at altitudes less than 80 km; and photographic records from the Precede I experiment are examined to determine the carrier of the long lived, electron-beam-induced chemiluminescence in the vehicle trail. Each of these topics is covered separately in the four subsections which follow.

EXCEDE SPECTRAL:

EMISSION IN THE 4.5 TO 5 μM REGION

Prepared By:

F. Bien and W. Cheng
AERODYNE RESEARCH, INC.
Bedford Research Park
Bedford, MA 01730

INTRODUCTION

The emission of NO^+ in the 4.3 μm band has been of great interest in understanding the infrared signatures during auroral and other electron disturbed environments. Because of the very bright emission from the ν_3 band of CO_2, however, emission from NO^+ during natural auroras is difficult to differentiate. The diatomic nature of NO^+ plus the shift in wavelength due to hot bands, however, have separated the NO^+ emission from the CO_2 region during the EXCEDE: Spectral experiment.

The emission of NO^+ during this experiment is compared to emission recorded from both liquid N_2 cooled InSb circular variable filter (CVF) detector operating between 3.25 and 5.4 μm and a liquid helium cooled CVF operating between 3.5 and 7 μm. The major contributors in this wavelength interval are CO_2, CO, NO^+, N_2O, and NO. Water was also observed at 6.3 μm by the liquid He cooled CVF. This signature was attributed to outgassing from the vehicle skin.

In the following sections, the data obtained from EXCEDE: Spectral will be compared to synthetic spectra generated for the possible emitters between 4.3 and 5 μm. Model calculations of the relative intensities of the possible emitters will be presented and compared to the CVF measurements.

EMISSION MEASUREMENTS BETWEEN 4.3 μm and 5 μm FROM EXCEDE SPECTRAL

The EXCEDE: Spectral experiment was carried out at Poker Flats, Alaska at 5:46 UT on 19 October 1979. A vehicle carrying an electron beam accelerator system consisting of four electron guns, each operating at 3 kV and 7 amps was launched south to north in a trajectory having a horizontal velocity of 300 m/sec and an apogee of 128 km. The electron beam system and instrument payload was separated from the accelerator at 37 km, and the payload followed a ballistic trajectory through the major portion of the experiment. The electron beam generation system was initiated at 133 seconds into the flight,

which went through its apogee at 188 sec. During the majority of the flight, only one electron gun was operating, providing a dose of 3 kV and 7 amps. The electron accelerator operation history on the downleg of the flight is shown in Figure 1.

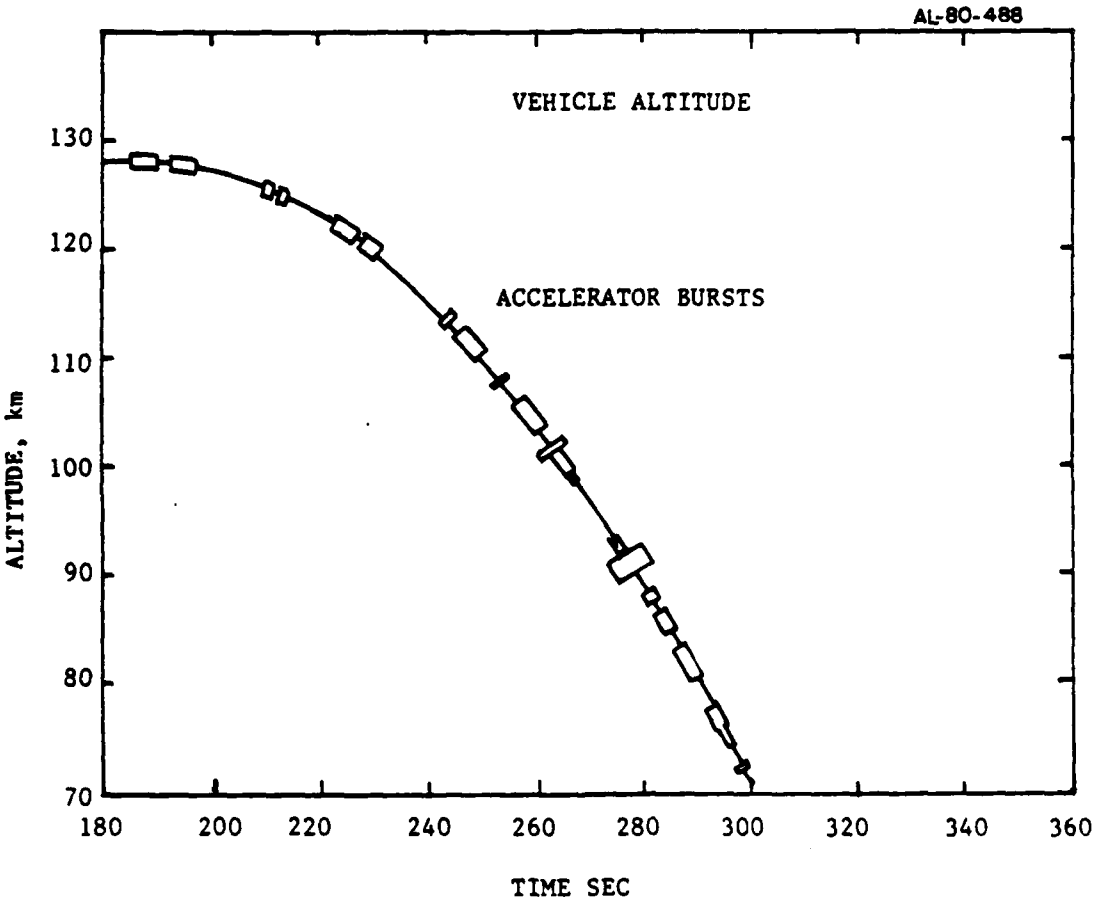

Figure 1. Electron Accelerator History Recorded from 3914 nm Emission.

In order to study the production of NO^+ emission from its 4.3 μm vibrational bands, particular attention was paid to the spectral region to the red of the identifiable $CO_2(\nu_3)$ band centered at 4.26 μm and to the blue of the NO 5.3 μm band. This region was covered by both the short wave CVF which covered from 2.2 μm to 5.4 μm in two segments, overlapping the region between 3.2 μm and 3.5 μm to give a spectral consistancy check, and a long wave CVF which covered two regions, 3.5 μm to 7 μm and 12 μm to 22 μm. Each CVF had both a high gain channel and a low gain channel, which provided measurements when the high gain channel went into saturation. A schematic diagram of the relative locations of the CVFs is shown in Figure 2. Also shown are the relative inclination angles of the electron beam accelerator, the geomagnetic field to which the electrons align, and the angular fields-of-view of the CVFs.

A typical CVF trace is shown in Figure 3. This trace, taken at 91.5 km on the down leg, shows a saturated $CO_2(\nu_3)$ peak, two secondary peaks at 4.55 and 4.65 μm, and a rise in signal just above 5 μm, attributed to NO formed in the experiment. At an altitude of 103 km, shown in Figure 4, the $CO_2(\nu_3)$ peaks comes out of saturation. The double peaks at 4.5 and 4.65 μm become a single very broad peak at approximately 4.65 μm. A very clear spectra of CO was recorded during payload separation at 68 km, 300 seconds after launch, shown in Figure 5. This figure shows that the CO v = 1 to 0 transition is shifted from the 4.5 and 4.65 μm features and that both the P and R branches of the CO emission are discernable through the instrument bandpass of 0.07 μm. Excitation of higher vibrational levels of CO would wash out the band center feature of the spectrum. However, the band center would also shift to the red.

A montage of several SWIR CVF traces during electron beam pulses over the trajectory is shown in Figure 6. Similar traces obtained from the liquid He cooled CVF are shown in Figure 7. The feature of interest is

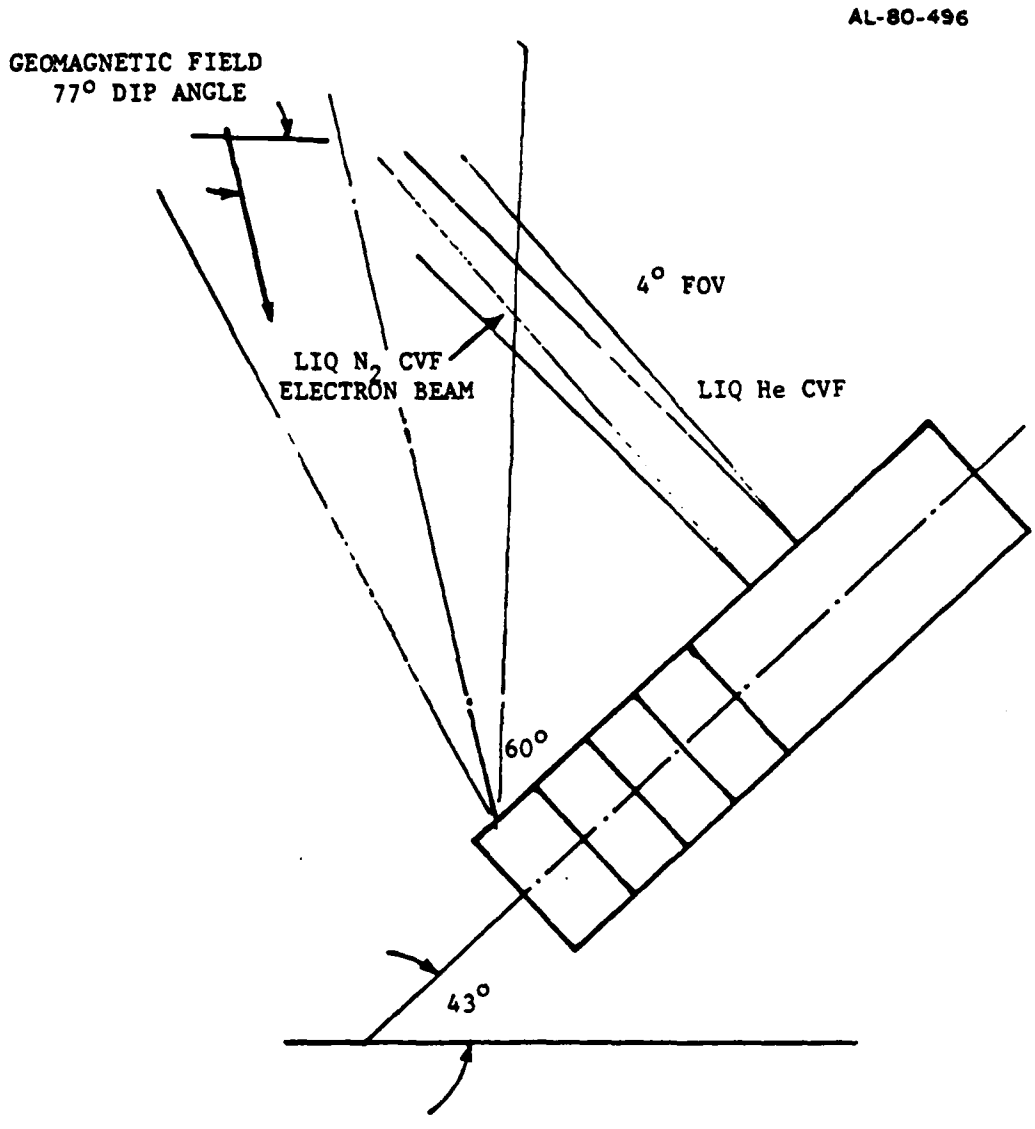

Figure 2. Vehicle Geometry and Alignment to Geomagnetic Field.

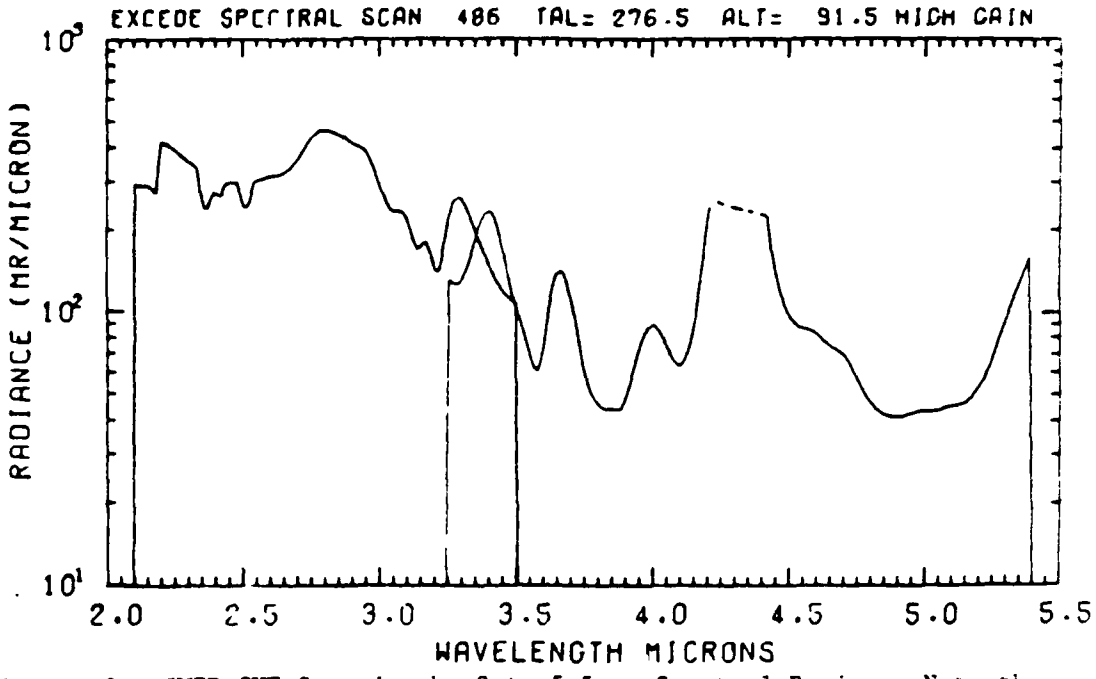

Figure 3. SWIR CVF Scan in the 2 to 5.5 μm Spectral Region. Note the Saturated CO_2 Peak, Followed by Two Peaks at 4.55 and 4.65 μm, Respectively.

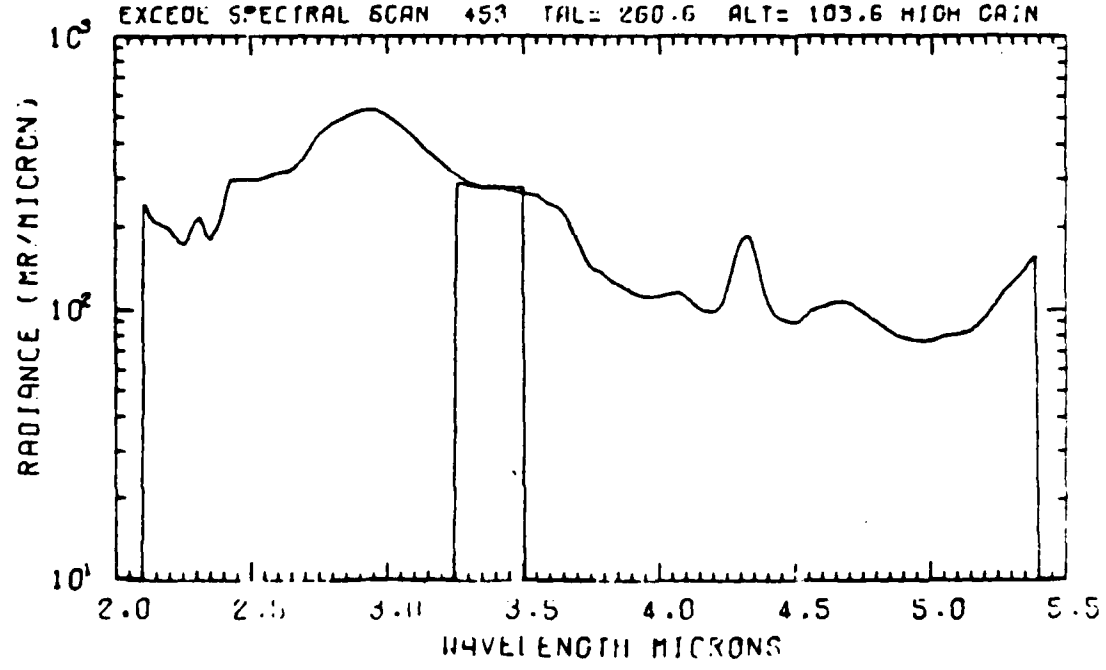

Figure 4. SWIR CVF Signature at 103.6 km. Note Unsaturated $CO_2\nu_3$ Peak, Second Peak at 4.65 μm.

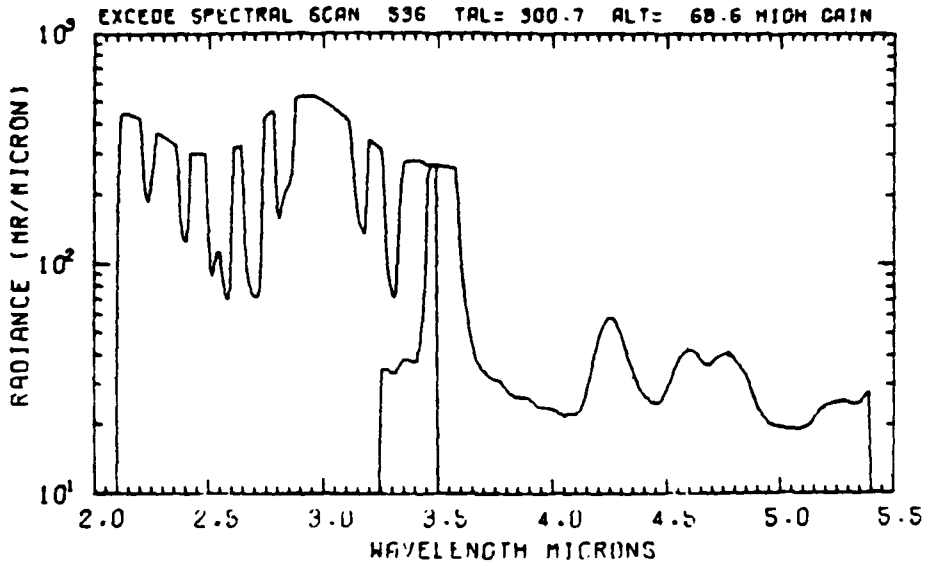

Figure 5. SWIR CVF Recording Separation of the Payload. Note the Unambiguous CO Band with Two Peaks, at 4.6 and 4.75 μm, Respectively, Matching the CO v = 1 to 0 Transition. Absolute Wavelength Calibration Appears to be About 0.05 μm High.

shown to peak at 4.65 μm on both CVFs. Taking the intensity at band center, the intensity profile is ratioed to the 3914 $N_2^+(1-)$ as a function of altitude in Figure 8. Note that this intensity increases with decreasing altitude except for a local maximum at 100 km.

EMISSION MODEL

The emission in the region between 4.3 μm and 5.0 μm can be attributed to four radiators: CO, CO_2, NO^+, and N_2O. The emission from CO_2 would be from the combination bands involving both bending and asymmetric stretch. These bands would track the CO_2 (ν_3) fundamental and could thus be ruled out as the mechanism causing the observed emission. The ozone overtone, at 4.8 μm was too far into the red to explain the spectral feature. O_3 was thus not considered in this model. The modeling of emission from the other

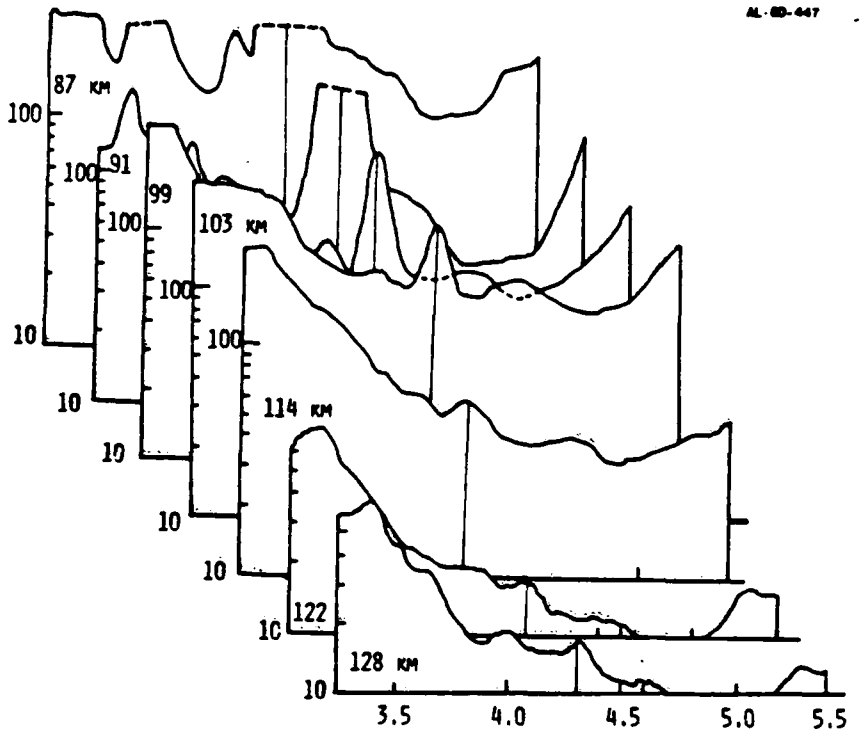

Figure 6. Montage of SWIR CVF Records from 3.25 to 5.5 μm Over Selected Altitudes Where Only Electron Beam Accelerator Number 4 Was Operating.

species were limited to reactions which were either directly or indirectly caused by the electron beam. Since these emissions dissappeared when the electron beam was off, the natural background was ruled out as the cause of these signals.

In order to obtain relative emission rates, a dose rate model was formulated. Since most of the emission arriving in the CVF is from the near field, only the high dose rates, in the vicinity of the electron beam, were monitored. The physical displacement of gun 4 from the two CVFs, however, meant that the very nonuniform dosing in the immediate vicinity of the electron gun is not the major contributor to the signal. Visible photographs

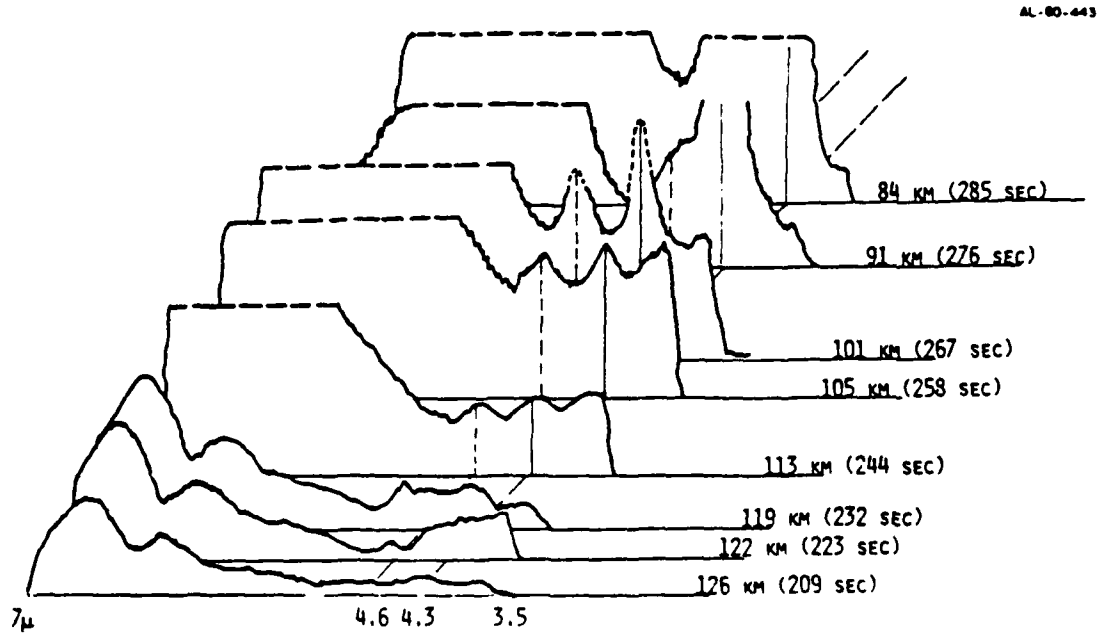

Figure 7. Montage of LWIR CVF Spectra Taken from 3.5 to 7 μm.

of the 3914 $N_2^+(1-)$ emission show that the emission is fairly uniform through the viewing path of the CVF. A uniformly dosed column is thus assumed. The dosing was assumed to form a cloud 30 m in diameter and $5.5 \times 10^{21}/n$ meters long, where n is the atmospheric density in m^{-3}. Here, the cloud length is defined when the intensity falls off by $1/e^2$. The intensity near the vehicle was assumed to vary as $I_o e^{-2x/L}$ where x is the distance from the vehicle. This scaling was obtained by looking at visible traces taken from ground based instrumentation of a 3 kV electron beam in PRECEDE (O'Neil, et al., 1977a). This cloud was assumed to be ionized at a rate equal to 3.75×10^{21} ion pairs per second (equal to a loss of 35 eV per ion pair, for a 3 kV, 7 amp electron beam). Of these, only a fraction was detected at any one time. Because of the 60 degree slant of the electron beam with respect to the CVF axis, the viewing path of the CVFs was assumed to be approximately 30 m. While these values

---

O'Neil, R.R., Bien, F., Burt, D., Sandock, J.A., and Stair, A.T., Jr., "Summarized Results of the Artificial Auroral Experiment, Precede", J. Geophys. Res. 83, 3273 (1978).

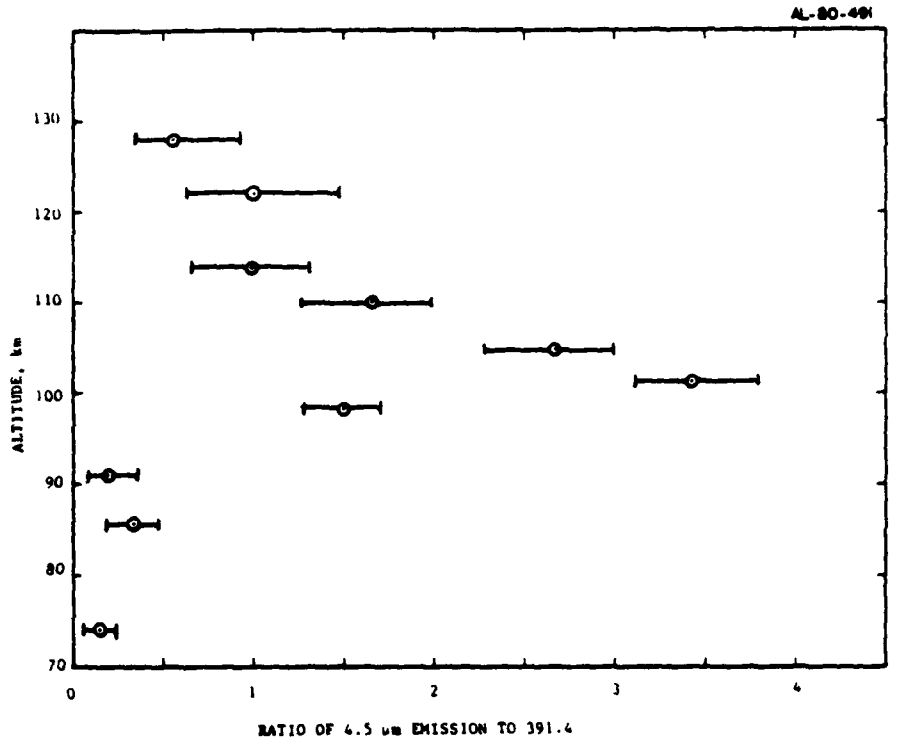

Figure 8. Ratio of Emission Feature at 4.65 μm to 391.4 nm Emission.

are somewhat uncertain, we see that as long as the collisional mean free path of the electrons with the atmosphere is at least as large the Larmor radius, that the electron beam excited region would be on the order of 15 m in radius. Using this simple model, the ionization rate along the field-of-view is given by the function.

$$P = \int_0^{x_o} P_o e^{-x/L}\, dx = 5.3 \times 10^{18}\left(1 - e^{-26/L}\right) \text{ ip/m}^2\text{sec} \qquad (1)$$

where L is given by

$$L = 2.77 \times 10^{21}/n \text{ (m)} \quad . \qquad (2)$$

Below 86 km the electron beam irradiated region is collisionally controlled, and a spherical, rather than cylindrical cloud is formed. This spheroidal cloud can be assumed to have the volume $\pi L^3/6$, giving the column ion production rate of $\pi L^2/6$.

The actual column ion production rate is monitored by looking at the 391.4 nm emission from $N_2^+(1-)$. The radiancy of this signal is obtained by taking a 0.07 chemiluminescent efficiency for N_2. Thus, the 391.4 is related to the collumn ionization rate by

$$391.4 \sim 0.07\phi_{N_2} P \quad , \tag{3}$$

where ϕ_{N_2} is the mole fraction of N_2 in the atmosphere. A plot of the N_2^+ (391.4) vs. altitude is shown in Figure 9.

The prompt formation for N_2^+, N^+, O^+, and O_2^+ is assumed to be proportional to the mixing ratios of the N_2, O_2, and O. The atomic ion N^+ is assumed to be produced in a one in four ratio to the N_2^+ production from N_2. A similar fraction of O^+ is assumed to be produced from O_2. In addition, O^+ is produced from the direct ionization of atomic oxygen. The relative formation rates due to primary electron excitation assumed in our model are listed in Table 1.

From these primary electron formed ions, charge transfer and ion transfer reactions take place which redistribute the ionization into ions having lower ionization potential. These reactions are listed in Table 2. Note that the primary formation mechanisms for NO^+ are from the ion transfer reactions $N^+ + O_2$, $N_2^+ + O$, and $O^+ + N_2$. During the course of the electron dosing, NO is formed from the reaction $N^2(D) + O_2$, which could provide a charge transfer channel for NO^+ formation. However, because of the rather short dosing times due to the motion of the vehicle, the amount of NO^+ formed through this channel is small compared to ion exchange.

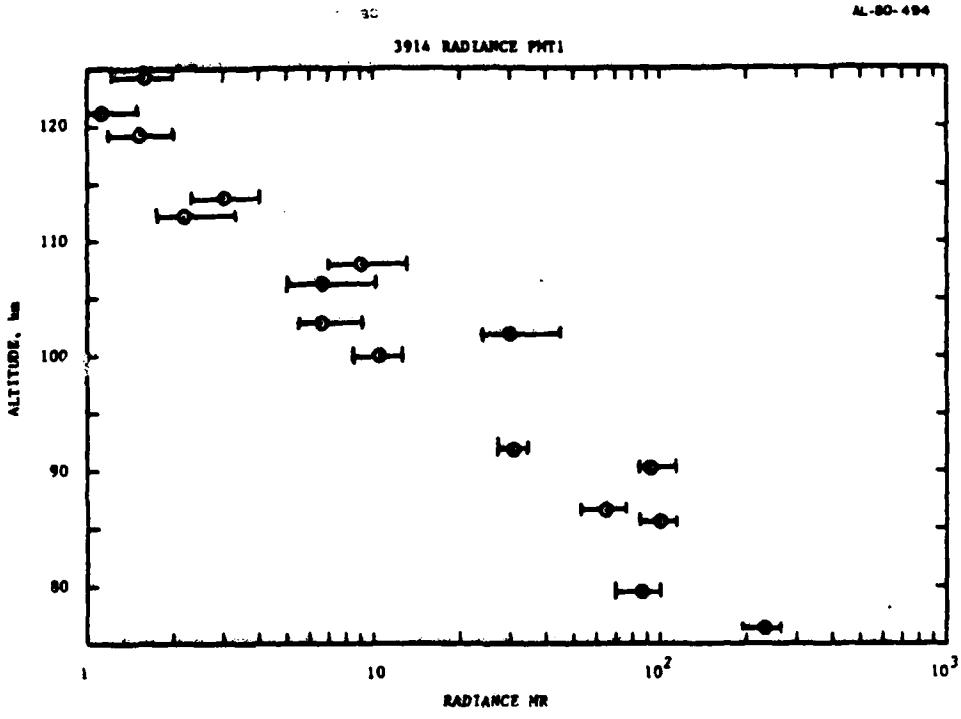

Figure 9. Radiance from 391.4 During EXCEDE: SPECTRAL.

Nitrogen is excited in the N_2 $A^3\Sigma_u^+$ level both by collision with primary electrons, and secondary electrons formed in the ionization process. In addition, a fraction of A state is formed from cascading from the first and second positive systems. For simplicity, we assume one $N_2(A)$ is formed for every N_2 ion pair formed. Thus, the $N_2(A)$ can be scaled to the N_2^+ (1st Neg) emission.

The excitation mechanisms of the three bands of interest, N_2O, NO^+, and CO, together with competition reactions to their formation and quenching of the excited states are listed in Table 3. The mechanism we attribute to the formation of N_2O is by the reaction $N_2(A) + O_2 \rightarrow N_2O + O$. The main source of competition is the quenching of $N_2(A)$ by atomic oxygen. Since this reaction

TABLE 1 - EXCITATION AND ION FORMATION BY PRIMARY ELECTRONS

	Ratio to N_2^+
$e_p + N_2 \rightarrow N_2^+ + e + e_p$	1
$e_p + N_2 \rightarrow N_2^+(B) + e + e_p$	0.087
$e_p + N_2 \rightarrow N + N^+ + e + e_p$	0.25
$e_p + N_2 \rightarrow N_2(A) + e_p$	1 ± 0.5
$e_p + O \rightarrow O^+ + e + e_p$	ϕ_O/ϕ_{N_2}
$e_p + O_2 \rightarrow O_2^+ + e + e_p$	ϕ_{O_2}/ϕ_{N_2}
$e_p + O_2 \rightarrow O + O^+ + e + e_p$	$0.25\phi_{O_2}/\phi_{N_2}$

is much faster than the N_2O formation reaction, N_2O is primarily produced at lower altitudes, where there is more molecular oxygen than atomic oxygen. N_2O formed by this reaction is 2.8 eV exoergic, therefore all three modes of vibration should be excited. We also assume that quenching by atmospheric species to be slow, thus calculate an optimistic N_2O vibrational intensity.

Carbon monoxide is not present in sufficient quantities in natural atmosphere to explain the observed signature if we assume that the observed signature to be from the direct excitation of CO. The direct excitation of CO,

$$CO + e \rightarrow CO^{\neq} + e \quad , \tag{4}$$

TABLE 2 - ION EXCHANGE REACTIONS USED IN MODEL

	Exoergicity	Rate
$N_2^+ + O \rightarrow NO^+ + N$	3.06 eV	$1.3 \times 10^{-10}(300/T)^{1/2}$
$N_2^+ + O \rightarrow N_2 + O^+$	1.96 eV	$1.0 \times 10^{-11}(300/T)^{1/2}$
$N^+ + O \rightarrow N + O^+$	0.92 eV	1.1×10^{-12}
$N^+ + O_2 \rightarrow NO^+ + O$	6.66 eV	2.8×10^{-10}
$N^+ + O_2 \rightarrow N + O_2^+$	2.50 eV	2.8×10^{-10}
$O^+ + N_2 \rightarrow NO^+ + N$	1.10 eV	1.2×10^{-12}
$O^+ + CO_2 \rightarrow CO + O_2^+$	1.22 eV	1.1×10^{-9}
$O^+ + O_2 \rightarrow O + O_2^+$	1.56 eV	1.5×10^{-11}

the CO would require concentration to be as high as 10^{12} cm^{-3} at 100 km altitude. A source of chemiluminscent CO is from the ion exchange reaction $CO_2 + O^+$ (Johnsen, et al., 1970). A very fast rate partially makes up for the low CO_2 concentration present, thus provides a possible source of CO emission. The concentration of CO_2 required to explain the signature can in part be due to vehicle outgassing. The atomic oxygen ion necessary for this source of CO is primarily produced by ionization of atomspheric O and dissociative ionization of O_2. The O^+ concentration, in turn, is controlled by charge transfer to O_2 and ion transfer with N_2 to form NO^+.

Johnsen, R., Brown, H.L., and Biondi, M., J. Chem. Phys. 52, 5080 (1970).

The formation of O^+ from ion transfer reactions is in general much slower than the direct production of O^+ from O and O_2, therefore contribute neglegibly to the CO formation during the EXCEDE experiment.

Formation of hot NO^+ is from the ion exchange reactions $N_2^+ + O$ and $N_2 + O^+$ at higher altitudes and from the reaction $N^+ + O_2$ at lower altitudes. Once NO^+ is formed in a vibrationally excited state, it may either radiate, or immediately dissociatively recombine with an electron. A second loss mechanism, that of collisional quenching by N_2, becomes comparable to dissociative recombination at altitudes below 86 km.

TABLE 3 - EXCITATION AND COMPETITION FOR EXCITATION OF SWIR ACTIVE SPECIES

N_2O:

$N_2(A) + O_2 \rightarrow N_2O + O$	1.5×10^{-12}	$A_{u\ell} = 258\ sec^{-1}$
$\rightarrow N_2 + O_2^*$	3.5×10^{-12}	
$N_2(A) + O \rightarrow N_2 + O(^1S)$	3×10^{-11}	

CO:

$CO + CO_2 \rightarrow CO + O_2^+$	1.1×10^{-19}	$A_{u\ell} = 34.7\ sec^{-1}$
$O^+ + O_2 \rightarrow O + O_2^+$	1.5×10^{-11}	
$O^+ + N_2 \rightarrow NO^+ + N$	1.2×10^{-12}	

NO^+:

See Table 2.	$A_{u\ell} = 31\ sec^{-1}$

SPECTRAL LOCATIONS OF EMITTERS

The relative spectral locations of N_2O, NO^+, and CO are very strongly dependent on their states of excitation. In particular, since they are formed through chemical reactions, their vibrational distributions are not expected to be thermal. Measurements of NO formed in the reaction $N^2(D) + O_2 \rightarrow NO + O$ have shown that that reaction was essentially equally distributed over all the possible vibrational levels. By taking a similar distribution for the exoergicity for each of the formation reactions, a synthetic spectra can be generated which would give the relative spectral locations of each of the radiators.

A plot of this synthetic spectra is shown in Figure 10. This spectra is plotted using 0.07 μm spectral resolution, approximately equal to the spectral resolution of the SWIR CVF in the wavelength region. The liquid He cooled LWIR CVF had a slightly higher spectral resolution in this region, therefore, would wash out the double peak shape of the CO completely.

Note that both the CO and NO^+ peaks can be shifted to 4.65 μm, where the observed radiation also peaks. The N_2O peak, however, would stay in the region of 4.5 μm.

As the 4.3 μm emission increases at lower altitudes, the center of the band becomes optically black, and the emission from the wings becomes important. Thus, the CO_2 band can spread into the 4.7 μm region. However, this band would not have an intensity peak at this wavelength. The combination band for CO_2 peaks at 4.85 μm, as would the overtone of O_3. These sources of emission would not explain either of the peaks shown in Figure 3.

COMPARISON OF PREDICTED INTENSITIES TO DATA

In order to estimate the relative intensities of the three emitters in the 4.5 μm region, the time dependent chemistry and synthetic spectra presented in the previous section together with the dosing levels assumed, were folded in with the speed of the vehicle. The dose time vs. altitude is shown in Figure 11. Above 95 km, the dose time increased with decreasing

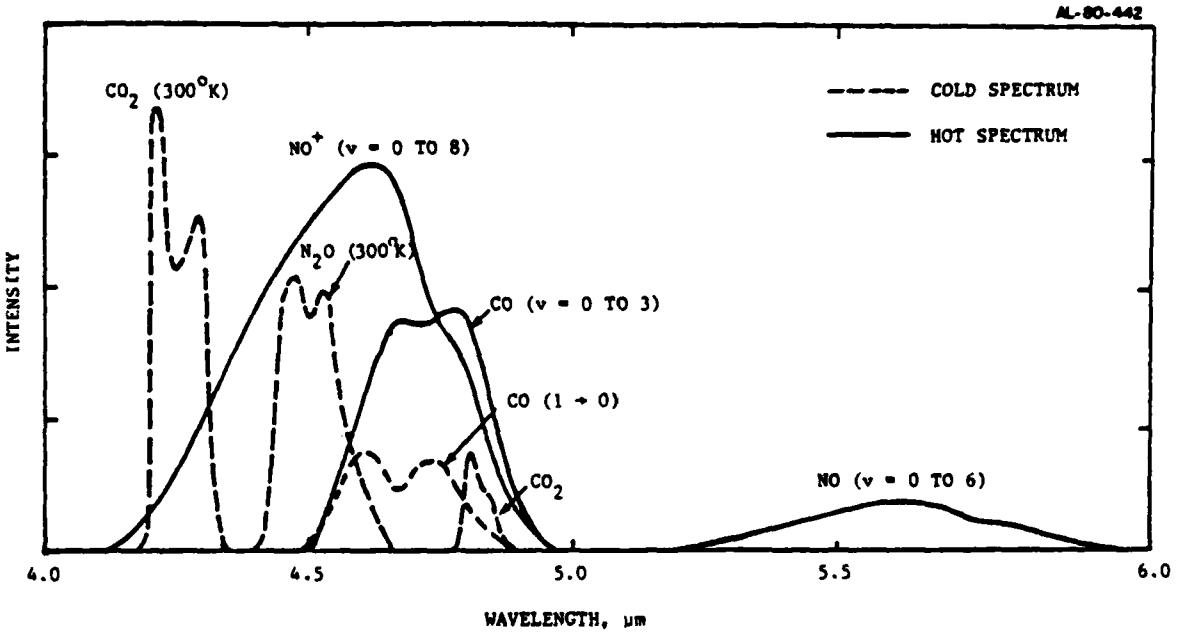

Figure 10. Synthetic Spectrum of Possible Emitters in the 4 to 5 μm Region.

altitude as the vehicle motion becomes more field aligned. Below 95 km, however, the vehicle velocity becomes so great that it flies out of the range of the electron beam in times short compared to the field crossing time.

Using the time scales presented in Figure 11 and the model presented in the previous sections, emission from NO^+, N_2, and CO are presented in Figure 12. Note the peaking with respect to altitude for both the CO and NO^+ emission intensities. This is due to the altitude dependence of O^+ and O, respectively. It was assumed that CO_2 was at a constant mixing ratio of 3×10^{-4}. This mixing ratio was supported by the $CO_2(\nu_2)$ emission spectra shown in Figure

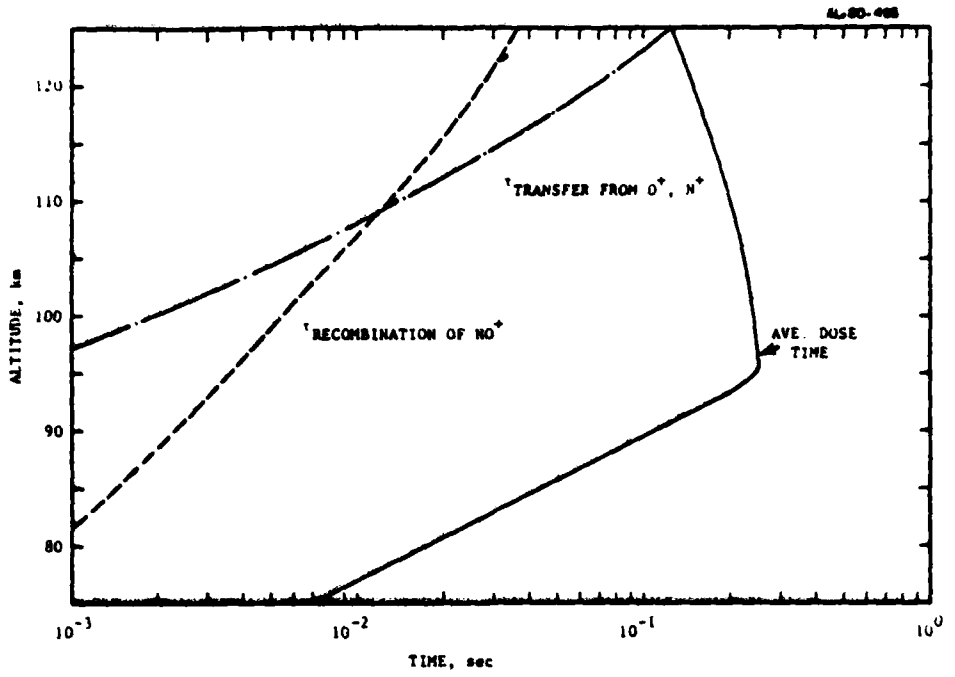

Figure 11. Comparison of Electron Beam Dosing Time to Times Required for Chemical Reactions.

13, which compared well with previous data taken by Rogers et al. Outgassing of CO_2 from the vehicle, if it was present, was not seen in the ν_2 emission, which was consistant with altitude profiles of the natural atmosphere. An upper limit for outgassing could nevertheless be inferred by the lack of CO_2 enhancement at apogee. Outgassing of CO_2 is thus limited to less than an average of 2×10^8 cm^{-3}, equal to the natural atmospheric concentration of 115 km.

Rogers, J.W., Stair, A.T., Wheeler, N., Wyatt, C.L., and Baker, D.J., "LWIR (7 - 24 μm) Measurements from the Launch of a Rocketborne Spectrometer Into an Aurora," AFGL-TR-76-0274 (1976).

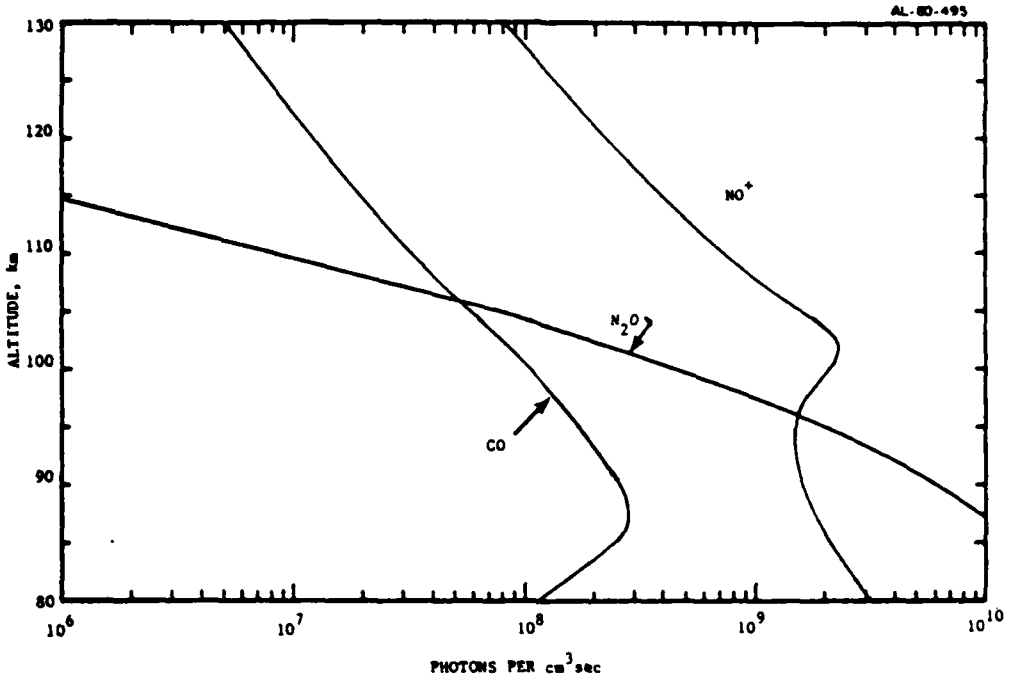

Figure 12. Specific Intensity Due to Emission from CO_2, NO^+, and N_2O, as Calculated from the Model.

The NO^+ emission is provided mainly by $N_2^+ + O$ at higher altitudes, thus follows the atomic oxygen concentration. Since a fraction of the nitrogen is dissociatively ionized, NO^+ is also formed at lower altitudes by $N^+ + O_2$. This source, in turn falls off with the O_2 concentration. An additional source of NO^+ is formed through $O^+ + N_2$. That reaction, however, is only one volt exoergic, and would therefore depend on the vibrational level of N_2 to provide vibrationally excited NO^+.

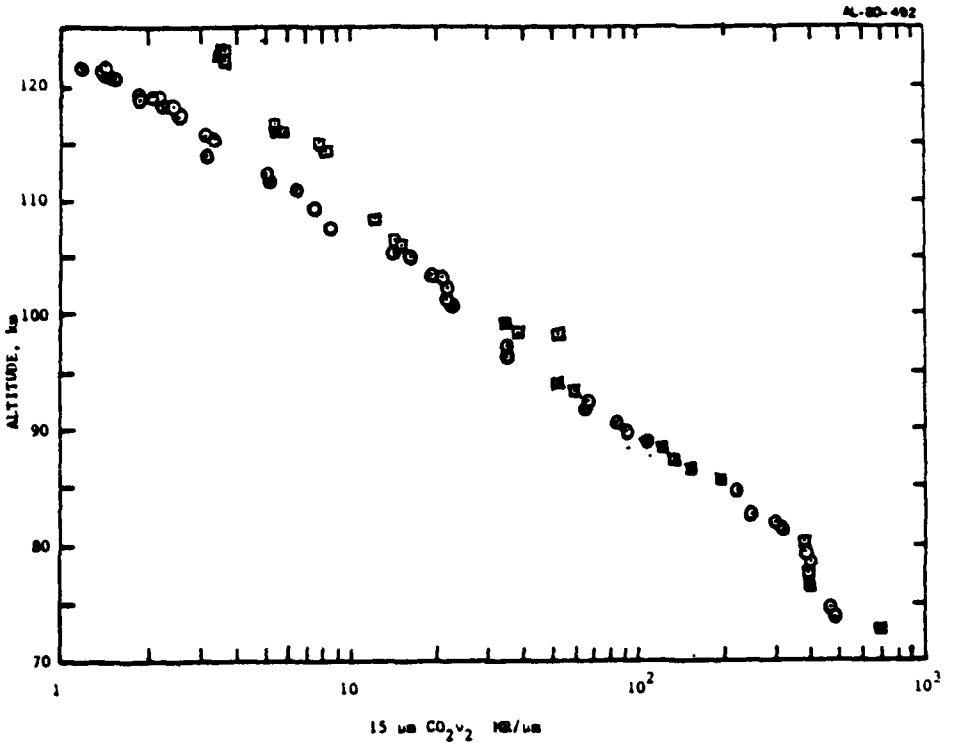

Figure 13. Emission Recorded from 15 μm CO_2 ν_2 at the Peak of the Band.

The N_2O produced, as discussed in the previous section, is through the reaction of $N_2(A) + O_2$. This signature, in turn, would scale with the O_2 density and the ionization of N_2.

The volumetric emission rate presented in Figure 12 can be compared to line-of-sight radiance by choosing an effective viewing path. Since the CVFs look perpendicular to the vehicle body, canted at 43° with respect to the vertical, and the geomagnetic dip angle is 77°; the look angle is approximately 60 degrees with respect to electron beam irradiated region. Using a beam radius of 15 meters, an effective viewing path of 30 m was assumed for comparisons of data to the model. The absolute viewing range may differ by

as much as a factor of 30% of this estimate, however, the relative viewing range would not change with altitude. These uncertainties can be further removed by comparing efficiency to 391.4 nm emission, as was shown for the actual data in Figure 8. This comparison for the model calculations is shown in Figure 14.

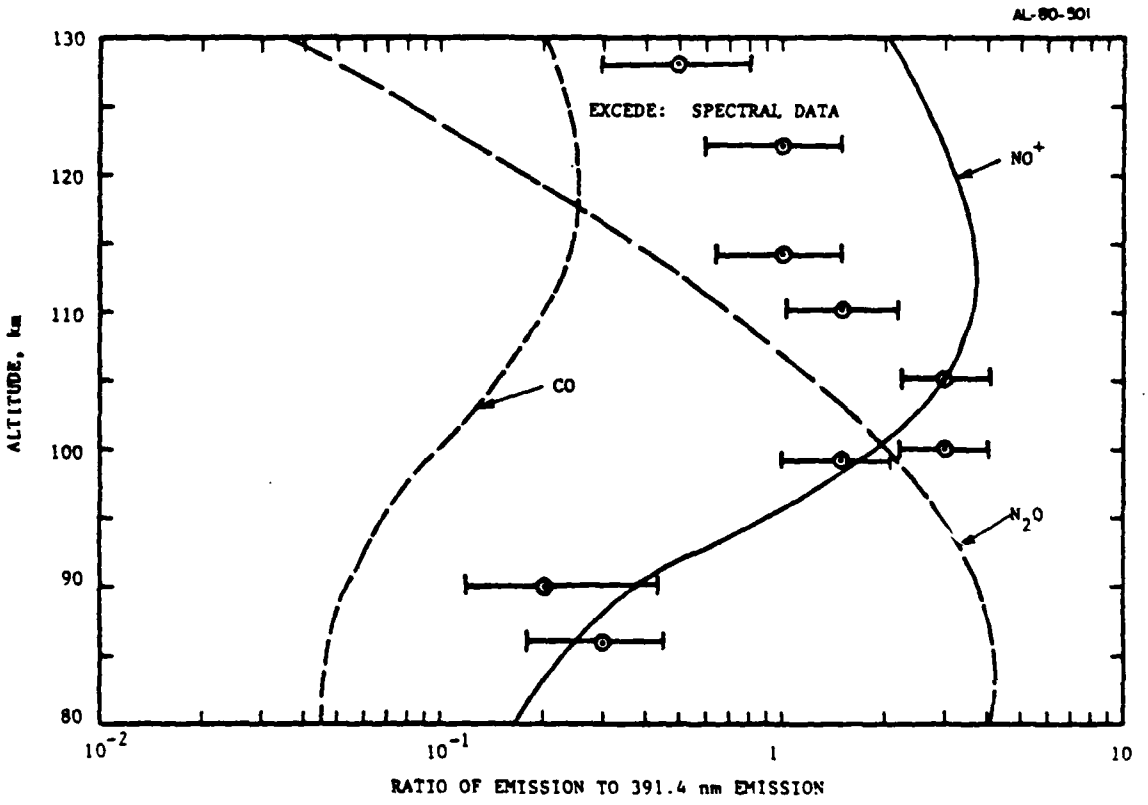

Figure 14. Comparison Between Calculated Emission and Data. Emission Intensities Plotted as a Ratio to 391.4 nm $N_2^+(1-)$.

CONCLUSIONS

The emission at 4.65 μm is shown to have an efficiency which would be too high to be from CO emission. Both the intensity and spectral bandshape are consistant with NO^+ emission from chemiluminescent ion transfer reactions. The second spectral peak at 4.5 μm appears to be consistant with N_2O emission, appearing as a shoulder at 103 km, and dominating the 4.65 μm peak at 91 km. The emission rate for this feature is much lower at low altitudes (<92 km) than would be predicted from our simple model, however, indicating either the quenching of $N_2O(\nu_3)$ eission or simply a smaller efficiency in producing N_2O vibrationally hot in the ν_3 band. The two other vibration modes, at 7.8 and 17 μm, respectively were not monitored, as they both fell in spectral gaps of the LWIR CVFs. Some emission from the 17 μm ν_2 N_2O band may have been recorded in the regions around the 17 μm gap, however.

The emission from NO^+ is considered somewhat a low estimate, as the reaction $O^+(^2D) + N_2$ was not included in the reaction set. This source of O^+ would add 3.7 eV to the reaction $O^+ + N_2$, providing enough energy to pump NO^+ to the higher vibrational levels needed for the observation. This source could also increase the CO signature if it provides a faster rate for dissociating CO_2.

The effect of H_2O on the quenching, excitation and formation of the infrared active species have not been considered. Even though an H_2O spectrum was measured, and attributed to outgassing from the vehicle, neither the absolute concentration of H_2O or the quenching rates are well established.

The emission ratio measurements when comparing the emission to $N_2^+(1-)$ at 391.4 nm is somewhat uncertain because absolute calibrations for the photometric instruments have not bee established.

The increased efficiency for emission at 4.65 μm at the altitude region around 100 km appears to be due to the reaction $N_2^+ + O$ forming NO^+. The quenching of NO^+ by N_2 decreases relative yields at lower altitudes. At higher altitudes, the dissociative recombination of N_2^+ rates becomes faster than the transfer rate to NO^+, therefore the NO^+ ratio to 391.4 emission again decreases.

During auroral storms, the ion densities would be much lower, therefore the efficiency of producing NO^+ chemiluminescence at 4.5 μm would in principle be more efficient. The formation of NO^+ through charge exchange with NO, however becomes an important channel for NO^+ production during those events.

While we have not proved conclusively that the 4.6 μm peak of the CVF spectra is from NO^+, there is strong evidence to suggest that vibrationally hot NO^+ was produced during EXCEDE: Spectral. Of the emitters thus far identified as possible emission candidates in this region, NO^+ is by far the most attractive.

LWIR CVF SIGNATURE ANALYSIS

Prepared By:

F. Bien and R. Lyons
AERODYNE RESEARCH, INC.
Bedford Research Park
Bedford, MA 01730

INTRODUCTION

Various portions of the wavelength dependent signature from the liquid Helium cooled Circular Variable Filtered (CVF) detector flown on EXCEDE: SPECTRAL are presented here. This CVF, using a HgCdTℓ detector, covered the wavelength region between 12 and 22 μm. An entire scan of this wavelength region was made once every second, covering the range in approximately 1/2 second. A typical signature trace during gun on conditions is presented in Figure 1.

While all of the CVF data have not been reduced as of this date, preliminary data analysis is presented in selected wavelength regions of the $CO_2(\nu_2)$ 15 μm band and the water rotation region between 17.5 and 22 μm. Also presented are altitude dependences for anomalous features at 14 and 16.2 μm, the former appearing only during beam on conditions and the latter appearing both during gun on and gun off.

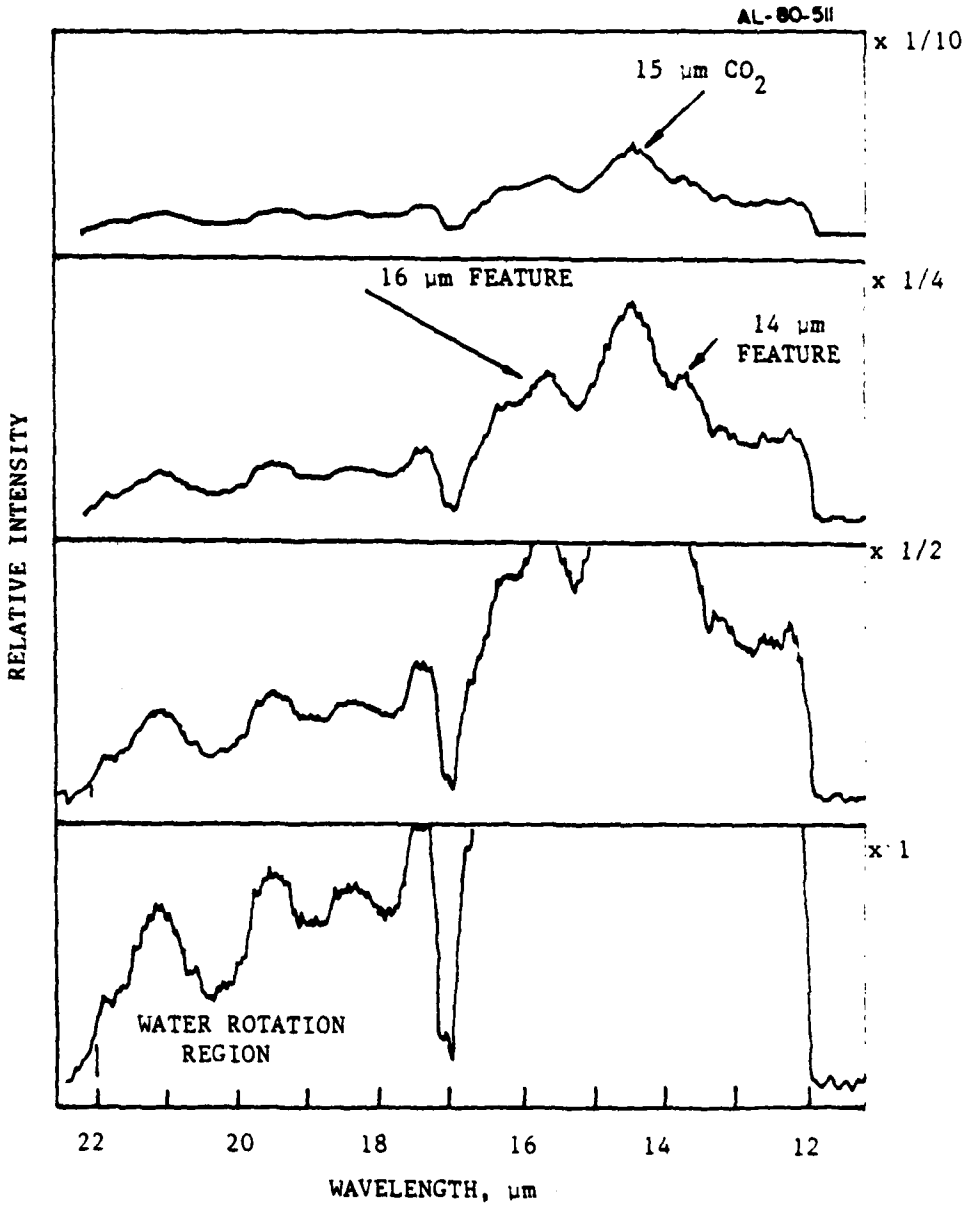

Figure 1. Typical Trace of LiHe Cooled CVF. This Data Taken During Gun on Conditions at 226 s. TAL, Altitude = 122 km.

ANALYSIS OF 15 μm EMISSION

The $CO_2(\nu_2)$ emission centered at 15 μm measured on EXCEDE: SPECTRAL was analysed as a function of altitude. The peak of this emission feature is shown for the downleg in Figure 2. The circles in Figure 2 represent the emission measured when the beam was off, while the squares represent the CO_2 signal when the beam was turned on. The width of the emission band also varied somewhat with altitude and dosing, and is shown in Figure 3. Plotted here is the full width half maximum points of the band taken from the raw data. An absolute wavelength calibration to this data is still somewhat uncertain, however, an approximate conversion of 1 mm equals 0.09 microns has been inferred.

The emission at 15 μm with beam off is very comparable to that measured in the 22 March 1973 aurora (Rogers, et al., 1976) as shown in Figure 4. This intensity is consistant with a constant mixing ratio model with CO_2 having a mixing ratio of 3×10^{-4} up through apogee. Outgassing from the vehicle skin could account for some of the signature at high altitude. This outgassing rate would not contribute to the signature at low altitudes because of the exponential density dependence on altitude. Because of the pathlength difference between any such outgassing and the scale height of CO_2 at these altitudes, an upper limit of 2×10^{9} cm^{-3} CO_2 distributed over 30 m can be present due to outgassing. This concentration becomes equal to the ambient concentration at 105 km.

The beam on conditions during the experiment, shown by the squares, do not deviate from the beam off conditions at low altitudes and is a factor of two larger than the beam off conditions near apogee (see Figure 2). Again, because of the path length difference between the beam excited region and the atmospheric scale height, the beam enhanced signature must be 100 times stronger than the natural signature before it can be detected. At lower altitudes, below 85 km, the signal becomes black. The only addition to intensity in this altitude regime would appear in a broadening of the band. In the intermediate altitudes, between 85 km and 110 km, any electron excitation of

Rogers, J.W., Stair, A.T., Wheeler, N., Wyatt, C.L., and Baker, D.J., "LWIR (7 - 24 μm) Measurements from the Launch of a Rocketborne Spectrometer Into an Aurora," AFGL-TR-76-0274 (1976).

the near black CO_2 band would provide a very small increase in band intensity. It is not surprising, then, that the beam enhanced CO_2 emission is only observable at higher altitudes. Unfortunately, the possibility of this enhanced signature being from electron beam excitation of CO_2 outgassing from the vehicle cannot yet be ruled out at these altitudes.

The increase in 15 μm CO_2 signature during electron excitation is thought to be due to the short lived complex CO_2^- formed between CO_2 and e^- (Boomerang model, Boness and Shultz, 1974). Their observations showed an energy loss spectrum at 3.6 eV having two progressions, namely the n00 and n10 modes. Further analysis is currently being carried out to analyse the extent of CO_2 excitation by this mechanism to compare with the altitude dependent enhancement observed.

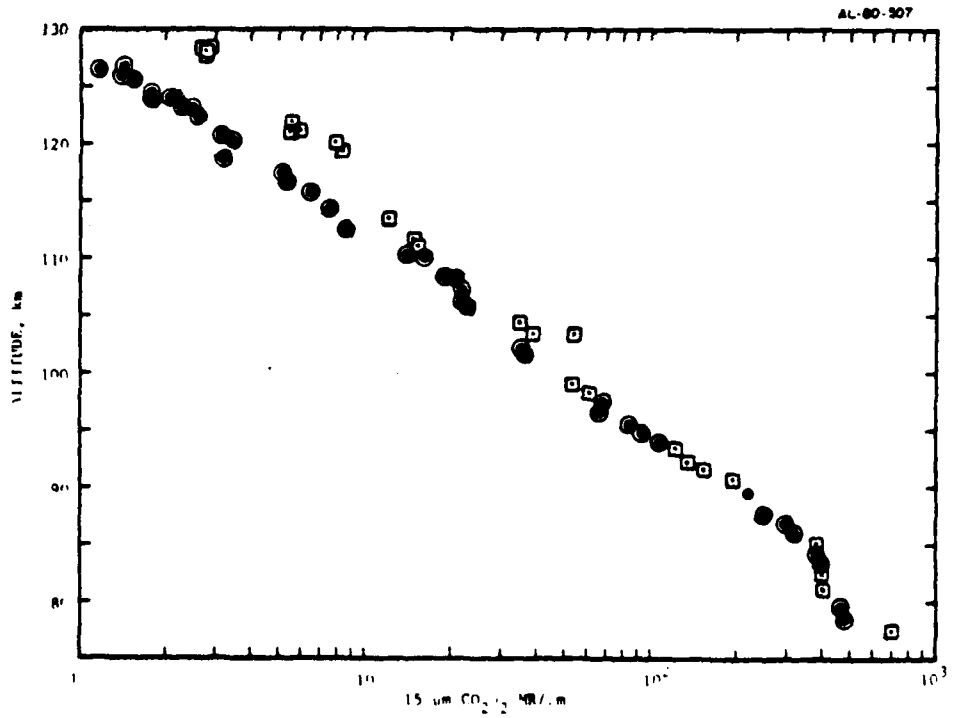

Figure 2. Emission Recorded from 15 μm $CO_2\nu_2$ at the Peak of the Band.

Boness, M.J. and Shultz, G.J., "Vibrational Excitation in CO_2 via the 3.8 μm Resonance," Phys. Rev. A 9, 1969 (1974).

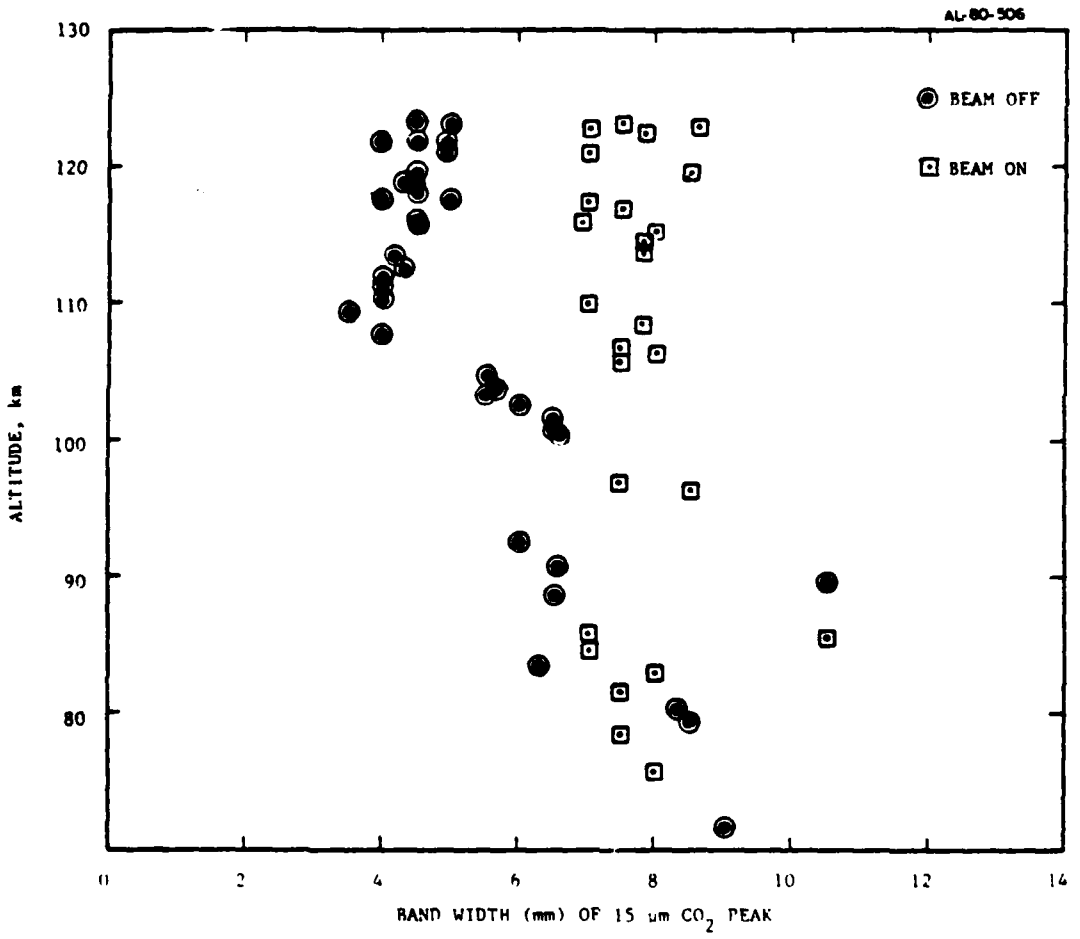

Figure 3. Bandwidth of $CO_2(\nu_2)$ Band as a Function of Altitude for Both Beam On and Beam Off Conditions. Note Relative Constant Bandwidth During Beam On and Variation With Altitude During Beam Off.

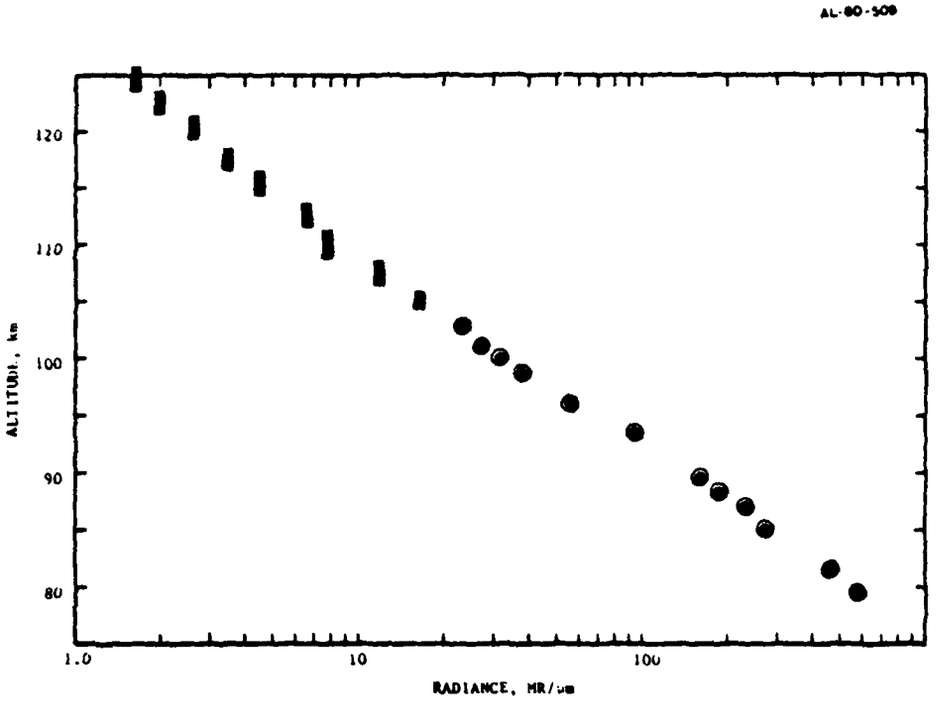

Figure 4. 15 μm $CO_2\nu_2$ Data of Rogers, et al., Measured During 22 March 1973 Auroral Event.

STRUCTURE IN THE 17 - 22 μm SPECTRAL RANGE

We conducted an analysis of the high gain CVF data in the 17 - 22 μm spectral range to determine the altitude dependence of both the positions and amplitudes of various peaks. The data indicate that there are two altitude regions over which the spectral peak locations are relatively constant. However, there exist significant differences in the peak locations between these regions.

At altitudes greater than about 90 km, structure was observed in the 17 - 22 μm range only when the electron beam was on. Representative examples of these data are given in Figure 5. Peak locations are constant for altitudes between 128 km and 90 km and the relative amplitudes of these peaks appear to be constant (with the exception of the "peak" at 17.5 μm). As the altitude decreases, the overall amplitude of these features increases.

The altitude dependence of the peak at 19.5 μm is plotted in Figure 6. The counting rate is computed with respect to the minimum at 20 μm. The decline in the counting rate below 105 km corresponds to an overall shifting of peak locations at lower altitudes.

Below 70 km spectral features again have fixed locations (which differ from the peak locations above 90 km) and their amplitudes increase with decreasing altitude. Furthermore, these features are observed whether the electron gun is on or not. Representative spectra in this altitude range are plotted in Figure 7. Comparison to the 300 K Hitran data (see Figure 8) indicates that the observed structure is due to H_2O.

If the structure above 90 km is also due to H_2O, then the H_2O must be outgassing from the rocket. Also, the rotational state population must differ significantly from that at 300 K, due to the changes in peak position and in relative amplitude in spectra below 70 km and above 90 km. The most obvious feature is 300 K H_2O peak amplitudes decline with decreasing wavelength, while the peak amplitudes increase with decreasing wavelength at

altitudes above 90 km. The relative intensity of each peak also changes. If this increase is due to heating of the H_2O by the electron beam, a local thermodynamic equilibrium calculation using a NASA H_2O band model would indicates that the H_2O temperatures involved must be between 2000 K and 3000 K.

It is planned that further analysis of this spectral range will include more detailed computations of the spectral structure arising from H_2O, to determine if the data above 90 km contains significant contributions from hot H_2O, and to perform a subtraction of the H_2O spectra from the data to uncover other peaks. Additional information may also be contained in the variation of the relative peak heights with altitude possibly pointing to different atmospheric emitters in this region.

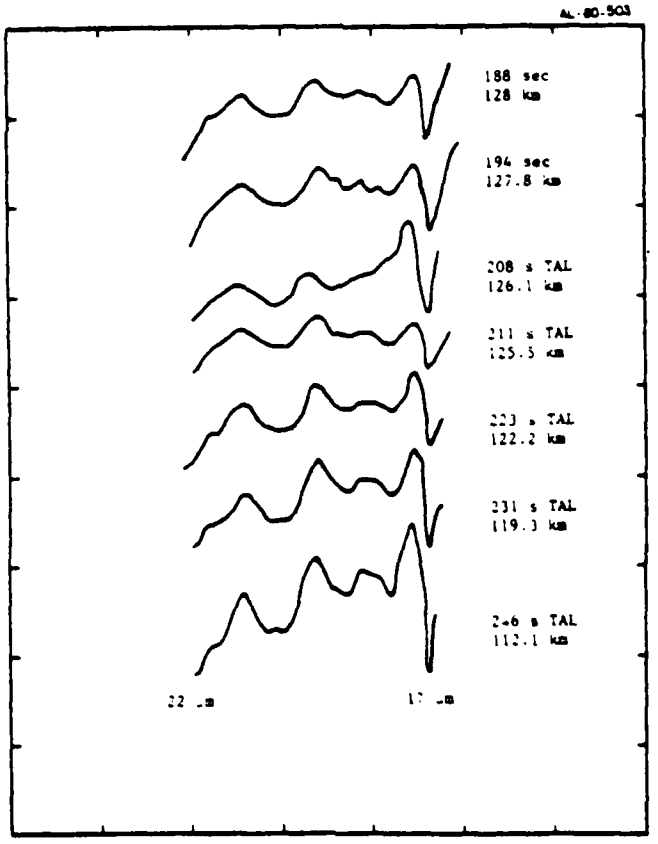

Figure 5. Emission in the 17 to 22 μm Region Observed at Altitudes Above 100 km. Note the Peaks at 20.8, 19.2, and 18 μm.

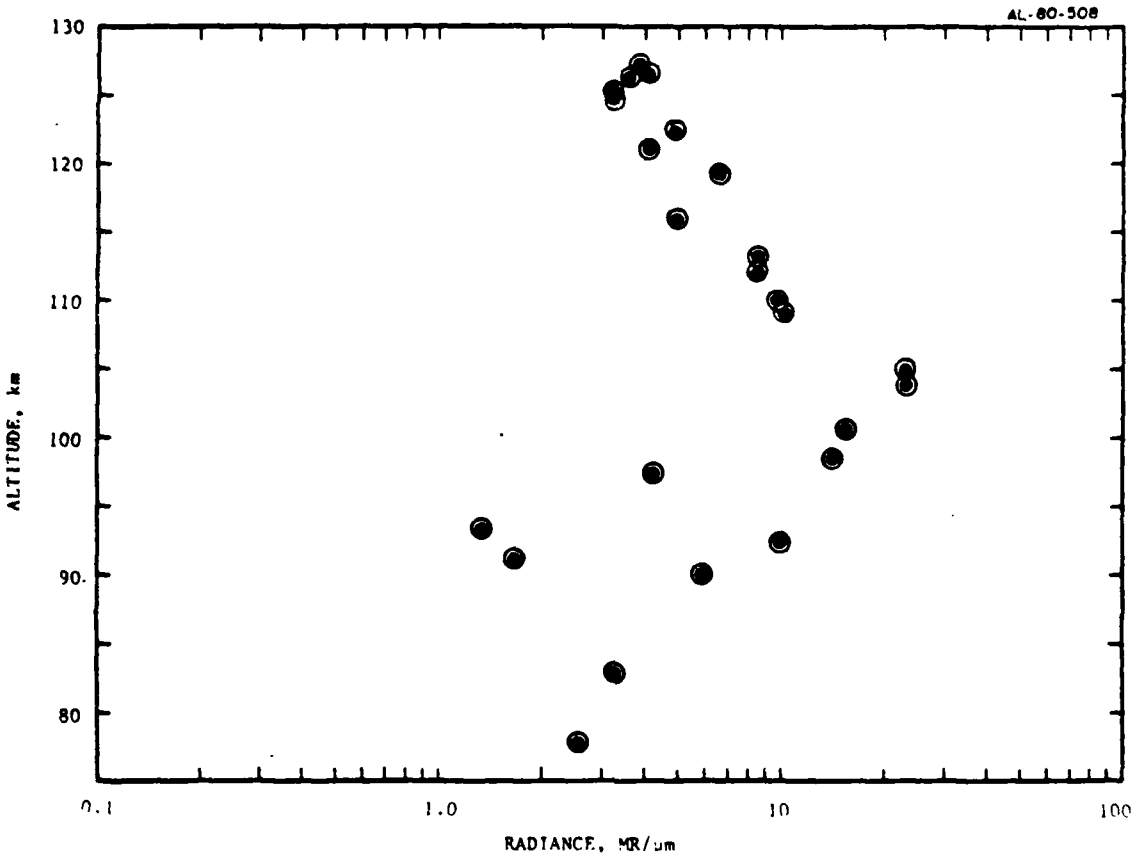

Figure 6. Altitude Dependence of the Peak Intensity of the 19.5 μm Spectral Feature.

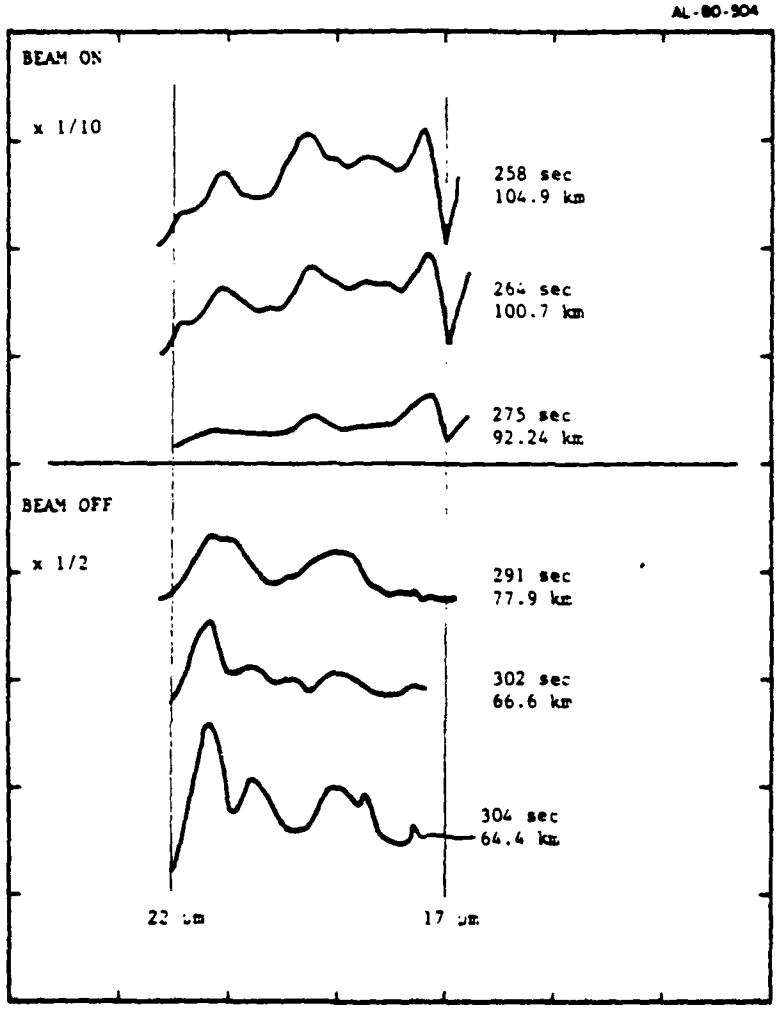

Figure 7. Emission Spectra at Low Altitudes Compared to Beam On Data at High Altitudes. Note Wavelength Shift in Spectral Peaks.

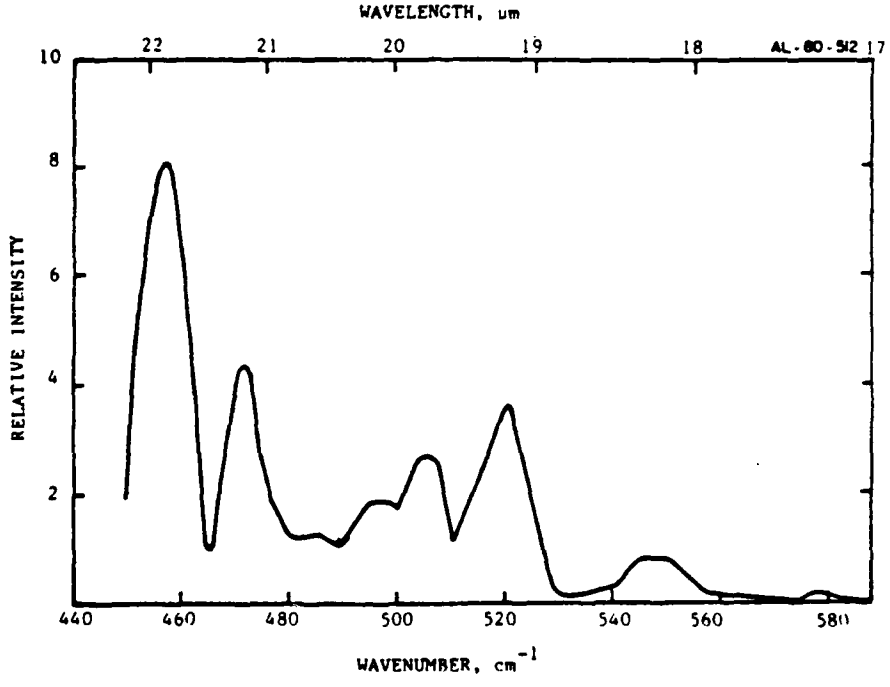

Figure 8. Synthetic Spectra of 300°K Water Rotation Using a 10 cm^{-1} Bandwidth Over Hitran Rotational Listings.

OTHER SPECTRAL FEATURES

In addition to the very prominent CO_2 15 μm signature and the spectral features between 17 and 22 μm, the data showed two readily identifiable spectral features at 14 and 16 μm, respectively. While the 14 μm signature appeared only when the electron beam was on, the 16 μm signature appeared to be constant over the entire flight.

Figure 9 shows a typical trace near apogee during gun off conditions. In addition to the 15 μm $CO_2(\nu_2)$, there is a 16 μm spectral feature which appears two times stronger. This spectral feature appears to be invariant with altitude as plotted in Figure 10. Because of the altitude invariance of this signature, it is thought to be due to a contaminant outgassing from the vehicle. The specific contaminant has not yet been identified, however.

A potentially more interesting spectral feature appeared at 14.2 μm as shown in Figure 11. This feature appeared only during gun on conditions near apogee, and became masked by the 15 μm CO_2 band below approximately 110 km. The altitude dependence of this feature is shown in Figure 12. The large scatter in this data is due to the subtraction of the large CO_2 and continuum baseline from the spectral peak.

This spectral feature may be due to the combination band of CO_2 $10^0 0$ $01^0 0$, which would peak at 13.9 μm. The cross section for electrons exciting the $10^0 0$ mode of CO_2 by electrons has been measured by Boness and Shultz (1974) to be as high as 2×10^{-16} cm^2. This state can then either emit or transfer in the Fermi resonance to $02^2 0$, and emit at 16.2 μm.

An alternative explanation for this 14 μm spectral feature is a contaminant of Tungsten from the filaments of the electron guns. If the tungsten filament were contributing to the 14 μm signatures, a second spectral peak at 10.5 μm should also be present (Yoder 1974).

Yoder, M.J., "High Temperature Arc Studies of Infrared Radiation from Boron and Tungsten Oxides", J. Quant. Spec. and Rad. Transfer 14, 1317 (1974).

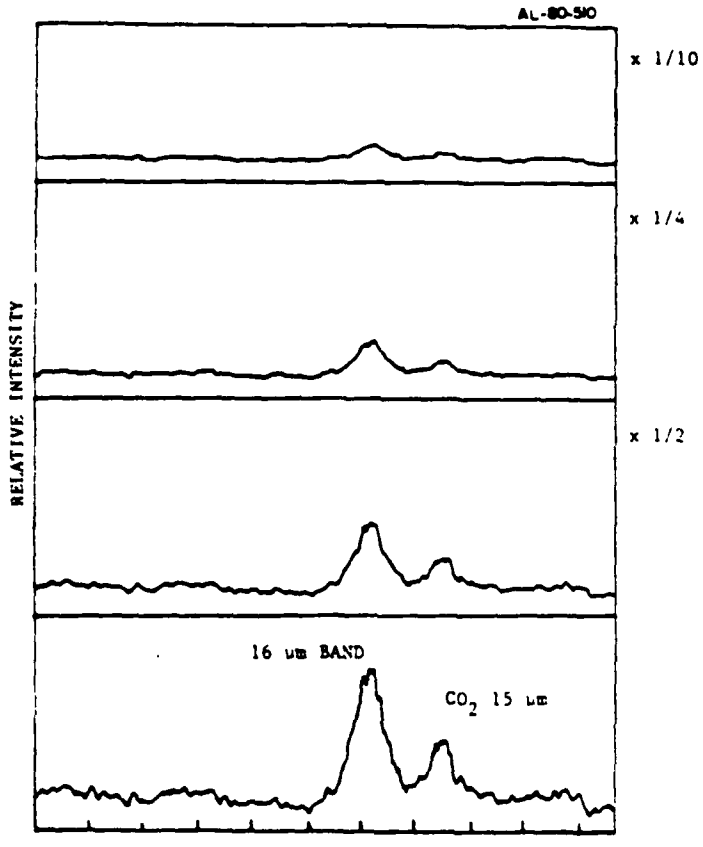

Figure 9. Anomolous Band Emission at 16 μm Taken From Lock-in Signal of LiHe CVF. Total Span is 12 to 22 μm.

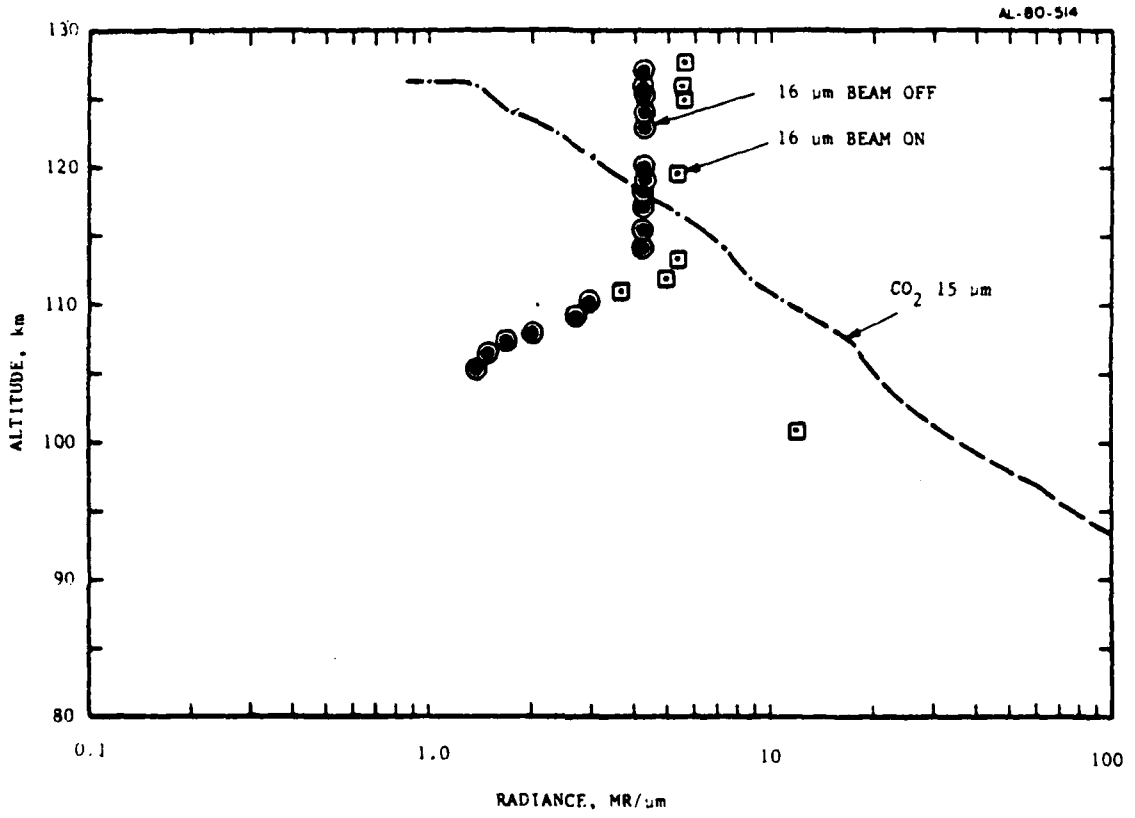

Figure 10. Altitude and Electron Beam Dependence of Anomolous Signature at 16 μm. Below 105 km, 16 μm Feature Dissappears into the $CO_2(\nu_2)$ Band Except for During a Single Record at 101 km.

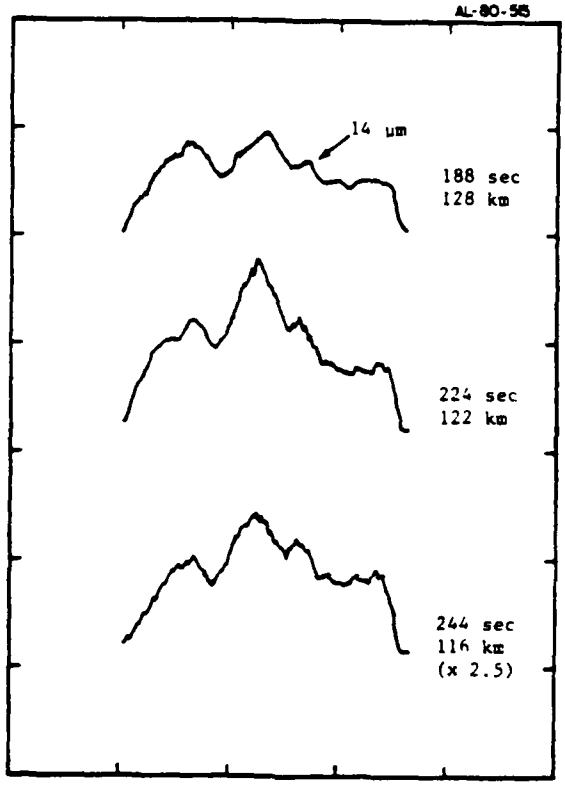

Figure 11. Representative Traces of 14 µm Emission Observed During Electron Dosing. Saturation of CVF High Gain Channel Prevented Observation of Peak Below 110 km.

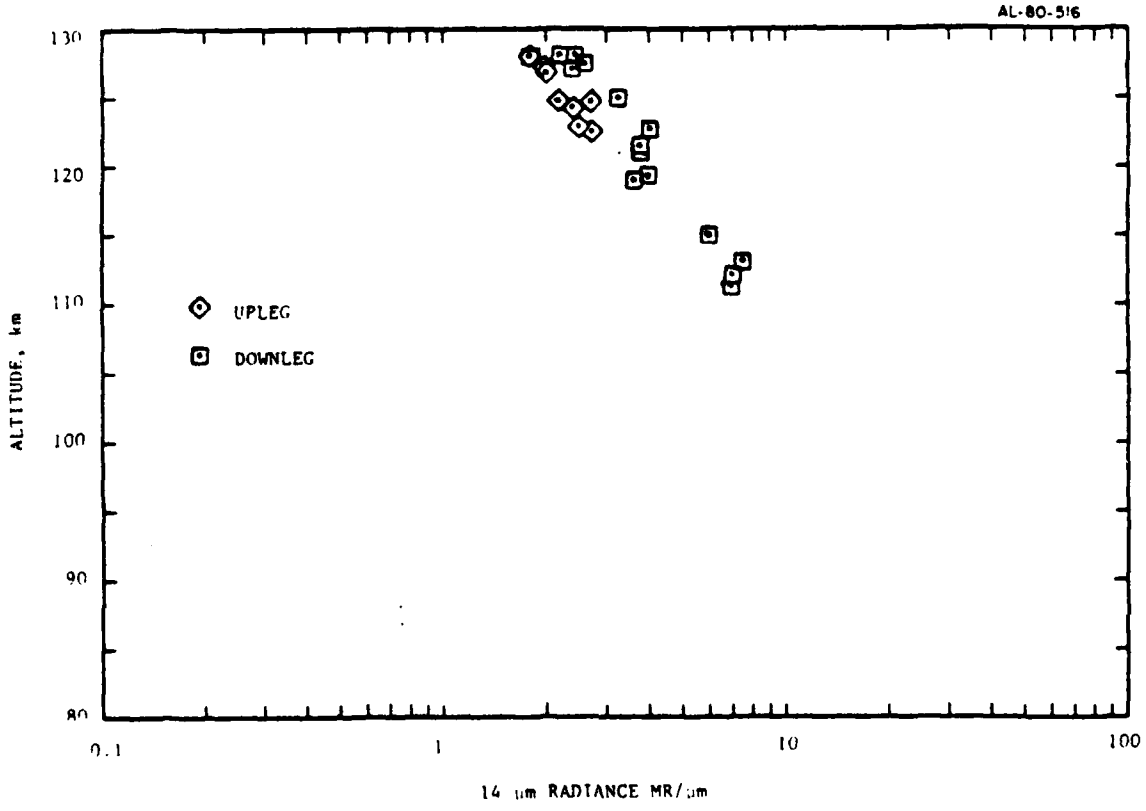

Figure 12. Emission from 14 μm Spectral Feature. Below 110 km the $CO_2\nu_2$ Saturates the High Gain Channel, Obscuring This Feature.

SUMMARY

The CVF data taken between 12 and 22 μm have been presented in a very preliminary form. The most obvious feature in this wavelength range is the $CO_2(\nu_2)$ bending mode radiation. This signature shows some enhancement at the higher altitudes. A detailed analysis, including effects of optical depth is yet to be performed on this signature.

Emission in the 17 to 22 μm region shows a definite electron irradiation as well as altitude dependence. While water rotation has not been completely ruled out as the source of this emission, water spectra at lower altitudes show that if H_2O rotation was present, it must take on a very different spectral distribution. High temperature water rotation spectra show a much more continuous variation in intensity, therefore, it can most likely be ruled out as the source of the emission.

The altitude profile for each spectral feature is currently being analysed. Since the separate peaks appear to have different altitude dependences, and their spacings are nonuniform, it is speculated that these features are from different emitters in the 17 to 22 μm region.

A peak at 17.5 μm observed on some traces at lower altitudes can be attributed to N_2O bending. However, because of a 17 μm notch in the CVF filter, this emission has not yet been analysed. Emission, however, does appear to peak on both sides of this notch, indicat a possibility of emission from the N_2O 17 μm band. Instrumentation factors, such as an initial overshoot due to phase lock errors have not been taken out of the data, therefore this data is not presented.

Emission at 16 μm appeared to be invariant with altitude above 115 km, 240 seconds TAL then dropping off sharply with time and altitude. This feature appears as time dependent as it is altitude dependent, therefore it may be attributed to some onboard contaminant. Below 108 km, this feature is swamped by the $CO_2\nu_2$ emission.

The spectral feature at 14 μm appears to be as noncontaminant emitter, as it varies with altitude. No data was taken below 110 km since the background radiation during gun on conditions saturated the channel. However, with further digitizing of the low gain channel of the CVF (a factor of 75 less sensitive), this signature may still appear at lower altitudes. Unfortunately, the $CO_2\nu_2$ band becomes so bright as to obscure this feature at very low altitudes where the low gain data was easily accessable.

PART 3

HYPERSONIC WAKE EFFECTS ON EXCEDE: SPECTRAL LOW ALTITUDE DATA INTERPRETATION

Prepared by

W. Cheng
Aerodyne Research, Inc.
Bedford Research Park
Crosby Drive
Bedford, MA 01730

INTRODUCTION

During the descent of the EXCEDE vehicle at lower altitudes (~80 km), electron beam excited atmospheric emission recorded by the on-board radiometric camera shows a stratified emission field (Figure 1). The regions of strong emission are due to the electron irradiation of the shock waves created by the vehicle. The analysis of the emission level from the atmosphere is thus complicated by the interaction of the electron beam with the flow field. What follows is a description of the general features of the flow field, and a quantitative estimate of the flow variables along a line of sight of the on-board radiometer. This information may be used in a detailed calculation of the electron beam induced radiation including the effect of the electron beam, flow field interaction.

THE FLOWFIELD AROUND THE EXCEDE VEHICLE AT LOW ALTITUDE

At low altitude the mean free path of the atmosphere is no longer large compared to the dimension of the vehicle and continuum flow effects become important. For discussion purposes and for comparison with the photographic record at 289 seconds after launch, we shall consider the flow field around the EXCEDE vehicle at 80 km altitude during descent.

At the altitude of 80 km, the mean free path is 4.4×10^{-3} m which is small compared to the vehicle dimension of ~1m. The vehicle is travelling at a downward velocity of 1000 ms^{-1} and a horizontal velocity of about 300 ms^{-1}. (The horizontal velocity is estimated based on a horizontal range of about 70 miles). In the reference frame of the vehicle, the free stream Mach number is 3.5, therefore a shock wave and wake system typical of hypersonic vehicles are created. The flow structure of hypersonic flow normal to a cylinder has been studied in References 1-5. Although in this case

---

[1]R.R. O'Neil, Ed., "EXCEDE SPECTRAL, Preliminary Results," AFGL-TM-41 (1980).
[2]D.S. Lykondis, "A Review of Hypersonic Wake Studies," AIAA J. 4, 4, (1966) pp. 577.
[3]J.F. McCarthy, T. Kubota, "A Study of Wakes Behind A Circular Cylinder at M = 5.7," AIAA J. 2, 4, (1964) pp. 629.
[4]W. Behrens, "The Far Wake Behind Cylinders At Hypersonic Speeds, Part I, Flowfield," AIAA J. 5, 12, (1967) pp. 2135.
[5]L. Lees, "Hypersonic Wakes and Trails," AIAA J. 2, 3, (1964) pp. 417.

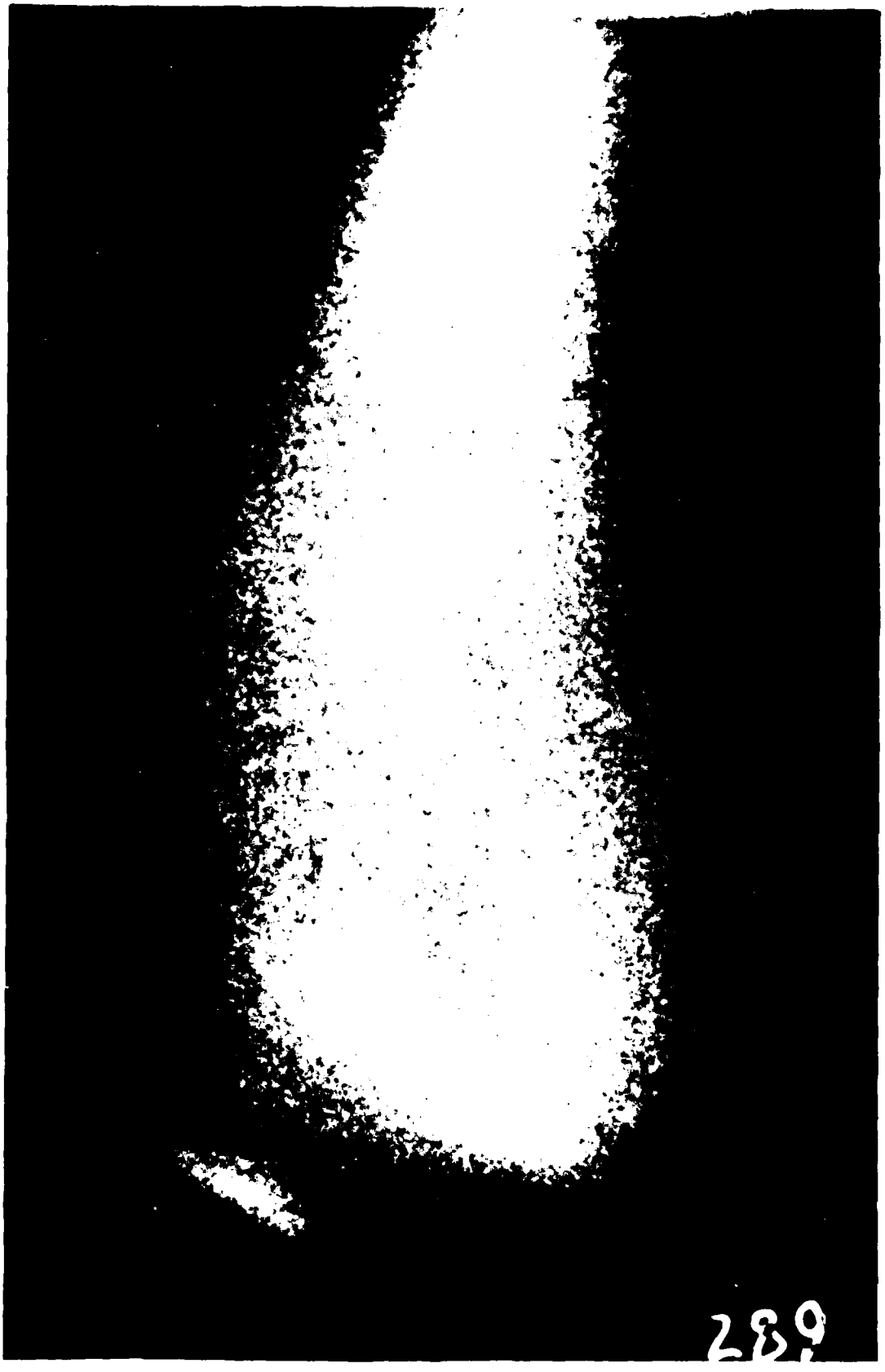

Figure 1. Electron Beam Irradiated Atmosphere.

the flow field is that of a yawed cylinder, the general flow features obtained from the literature are still applicable.

A typical three dimensional shock wave and wake system is shown in Figure 2. A transverse section and a longitudinal section of the flow field are shown in Figures 3 and 4. The flow field is characterized by a bow shock which wraps around the front surface of the vehicle and extends backwards. Behind the vehicle, there is a wedge-shaped recirculation region extending approximately three body diameters downstream. At the tip of this wedge-shaped region (Figure 4), the flow streams outside the vehicle boundary layer merge together, resulting in a high pressure and temperature "neck". For free stream Mach numbers greater than approximately 1.5, the flow behind the bow shock is overexpanded, and then re-equilibrates with the pressure at the wake region through a wake shock. Typically the gas is compressed above the free stream value by the bow shock, it then expands to a value below the free stream value, and then is recompressed by the wake shock to the value at the wake region. Such a profile is shown in Figure 5.

INTERPRETATION OF THE EMISSION PHOTOGRAPHS

Figure 6(a) is a photograph taken by the on-board radiometric camera at 80 km altitude when the master electron gun (Gun #1) is on. The photograph records the angular position in the field of view of the camera subtended by the electron beam irradiation. The corresponding physical dimensions in the plane along the beam direction and perpendicular to the plane of Figure 3 are shown in Figure 6(b). The features in the photograph may be identified with the flow structure around the vehicle though Figure 3, which is a scale drawing of the vehicle shock wave and wake system, the camera field of view, and the electron beam irradiation. The glow at the near end of the photograph corresponds to the irradiation of the wake neck region by the electron beam. The two bright bands at the far end of the photograph are a result of the interaction of the electron beam with the bow shock surface at the two ends of the vehicle.

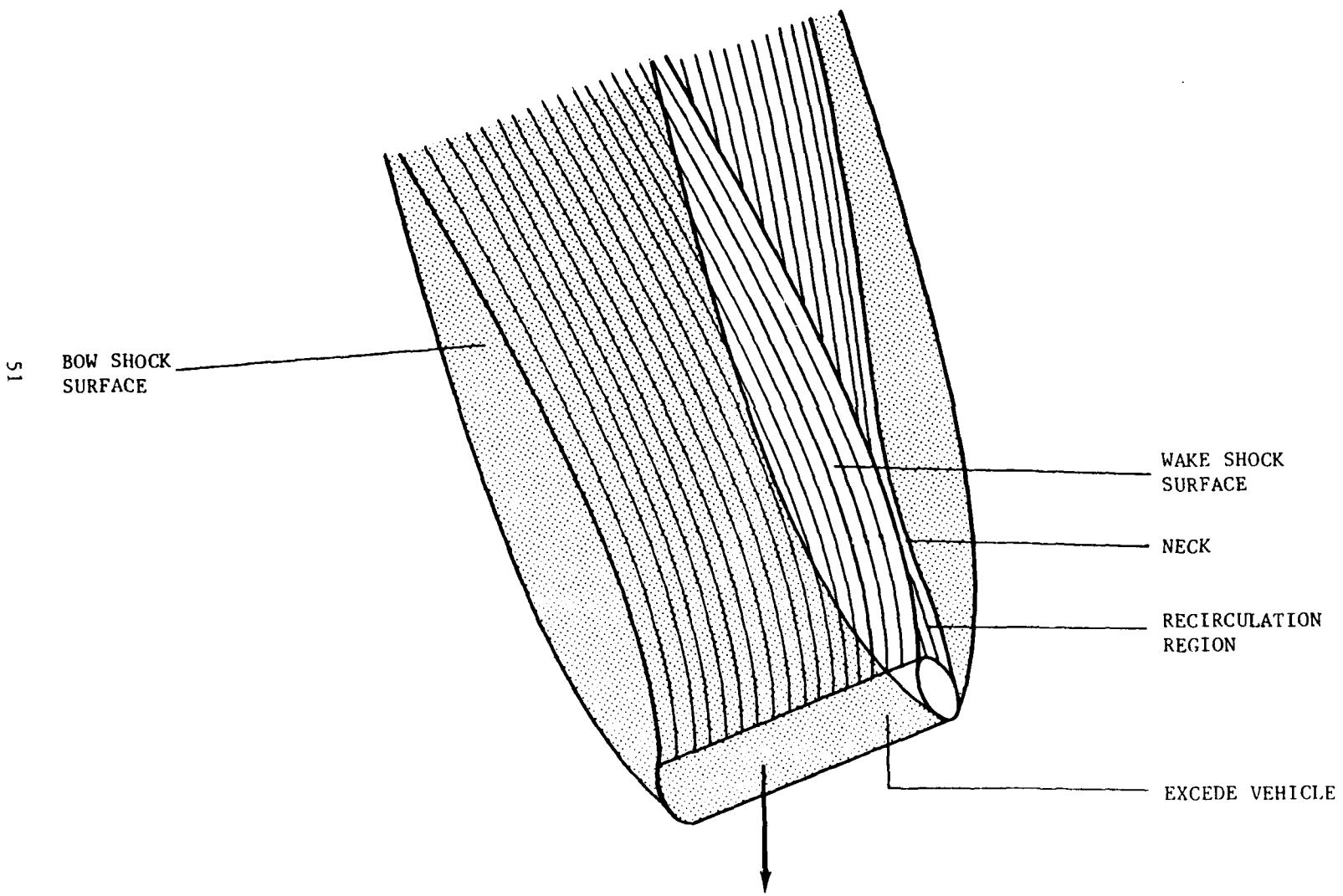

Figure 2. Shock wave and wake system of EXCEDE vehicle at low altitude.

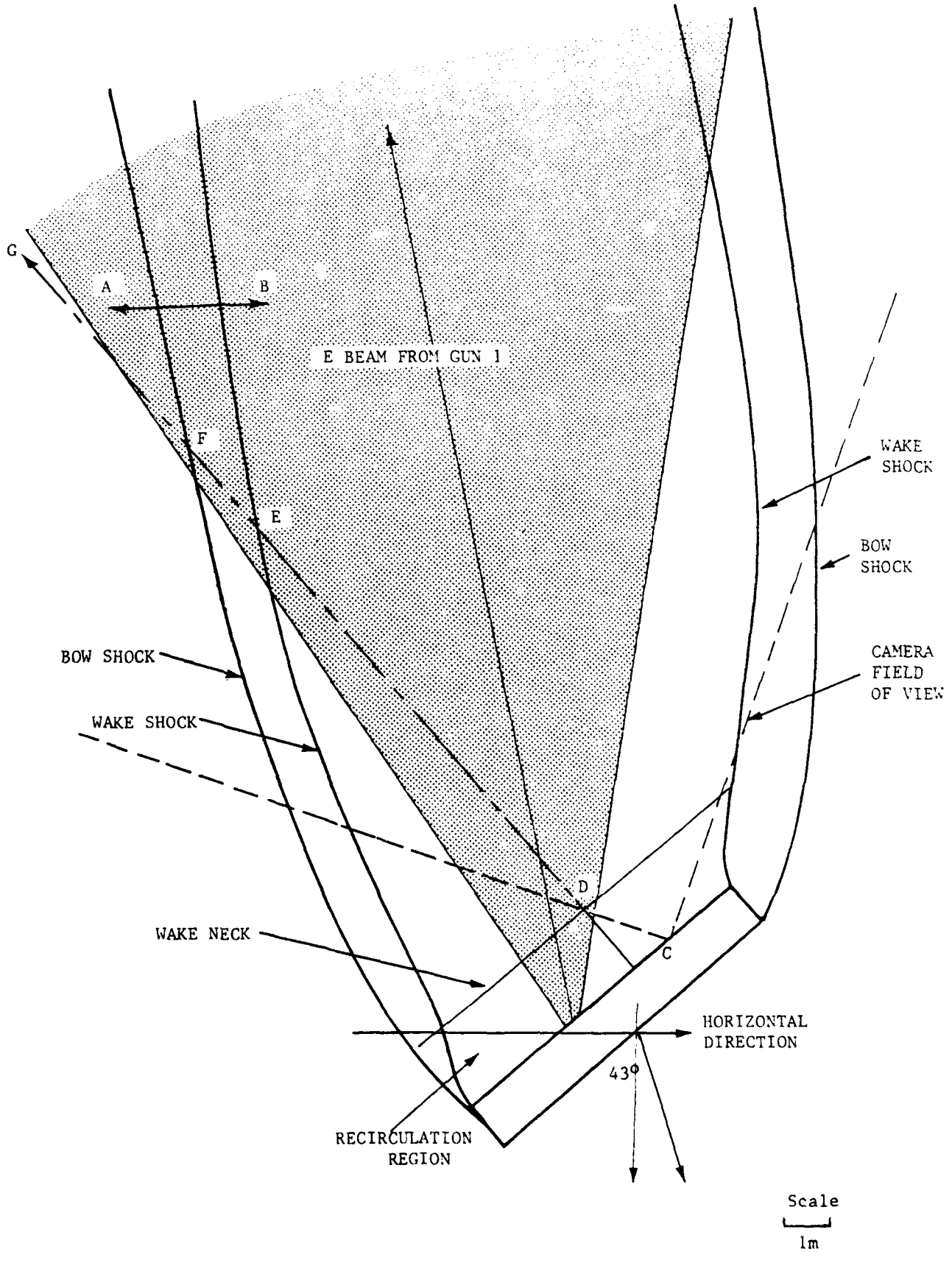

Figure 3. Shock wave and wake system of EXCEDE vehicle at low altitude, transverse section.

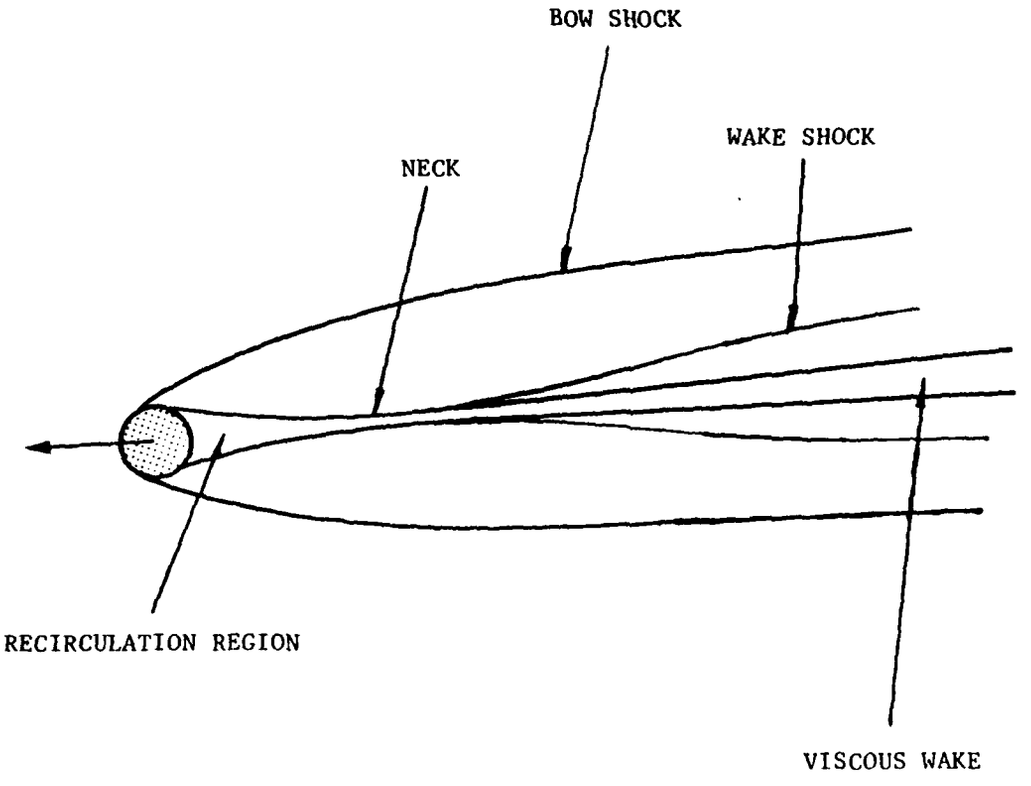

Figure 4. Wake system of EXCEDE vehicle, longitudinal section.

81-463

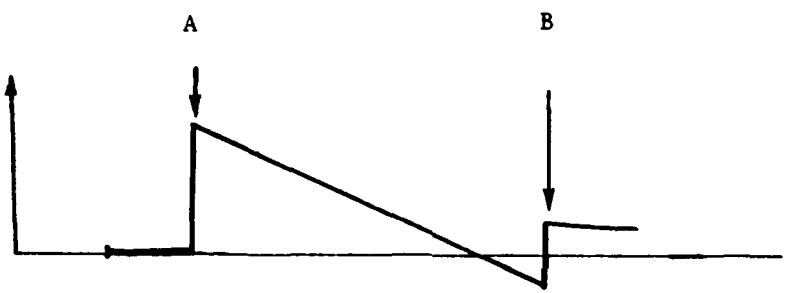

Figure 5. Typical density ratio profile across bow shock and wake shock. (Section AB of Figure 3)

(a)

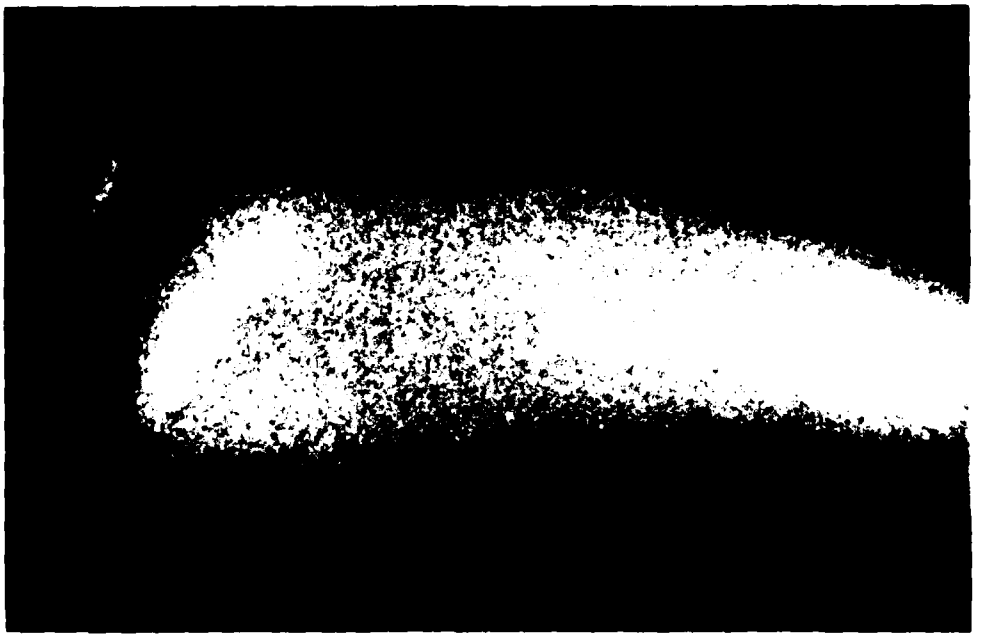

(b)

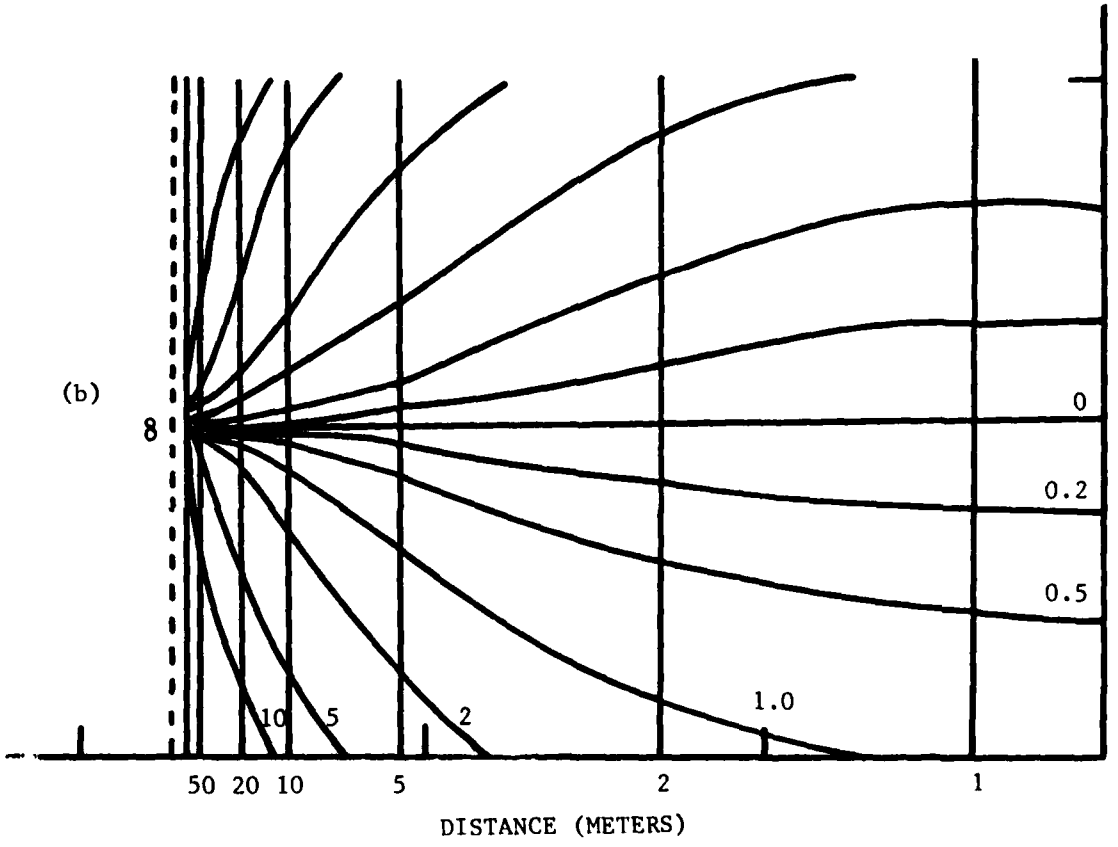

Figure 6(a). Electron beam excited atmospheric emission at 80 km.
(b). Distance grid corresponding to photo along the axis of the electron beam.

QUANTITATIVE DESCRIPTION OF FLOW FIELD

The flow variables along the line of sight may be described as follows. Referring to Figure 3, the line of sight CDEFG intersects the wake neck at D, the wake shock at E and the bow shock at F. Based on Figure 6, the positions D E and F are estimated to be 3, 10 and 12 body diameters downstream. Theoretical calculation of the flow field around the vehicle is a major task that is beyond the scope of the present study. The only detailed flow field measurement of a cylinder in hypersonic flow is that of Reference 3. The measurement was performed with $M_\infty = 5.7$ and with the cylinder normal to the flow. The result is summarized in Figure 7. The proper scaling of the $M_\infty = 5.7$ result to the present case which involves a yawed cylinder flow at $M_\infty = 3.56$ with important end effects is uncertain. Nevertheless, for a sensitivity analysis of the effect of wake and shock structure on radiation, it suffices to use the results of Figure 7.

The convection velocity may be calculated from the Mach number. The Mach number profile of Figure 7, however, must be scaled. The profile shows that the Mach number along the center line has recovered to the value at the edge of the wake shock for $x/d > 10$. We shall scale the Mach number profile by keeping the ratio of M downstream of the wake shock to M_∞ the same. For $M_\infty = 3.56$, the Mach number after the wake shock becomes 1.25.

The shock strength at the wake shock and at the bow shock depends on the shock inclination which is not well known. For this calculation, we take the inclination at the bow shock to be 30°. At $M_\infty = 3.56$, the density ratio becomes 2.33. At the wake shock, the Mach number behind the shock is 1.25. We take a deflection angle of 5°, which will give a density ratio of 1.20. The resulting density distribution is shown in Figure 8.

DISCUSSION

The profile in Figure 8 shows that the density at the wake is about half that of the free stream, but it jumps to a value twice that of the free stream value at the bow shock. To assess the effect of the density stratification, it is necessary to calculate the electron beam energy deposition at each

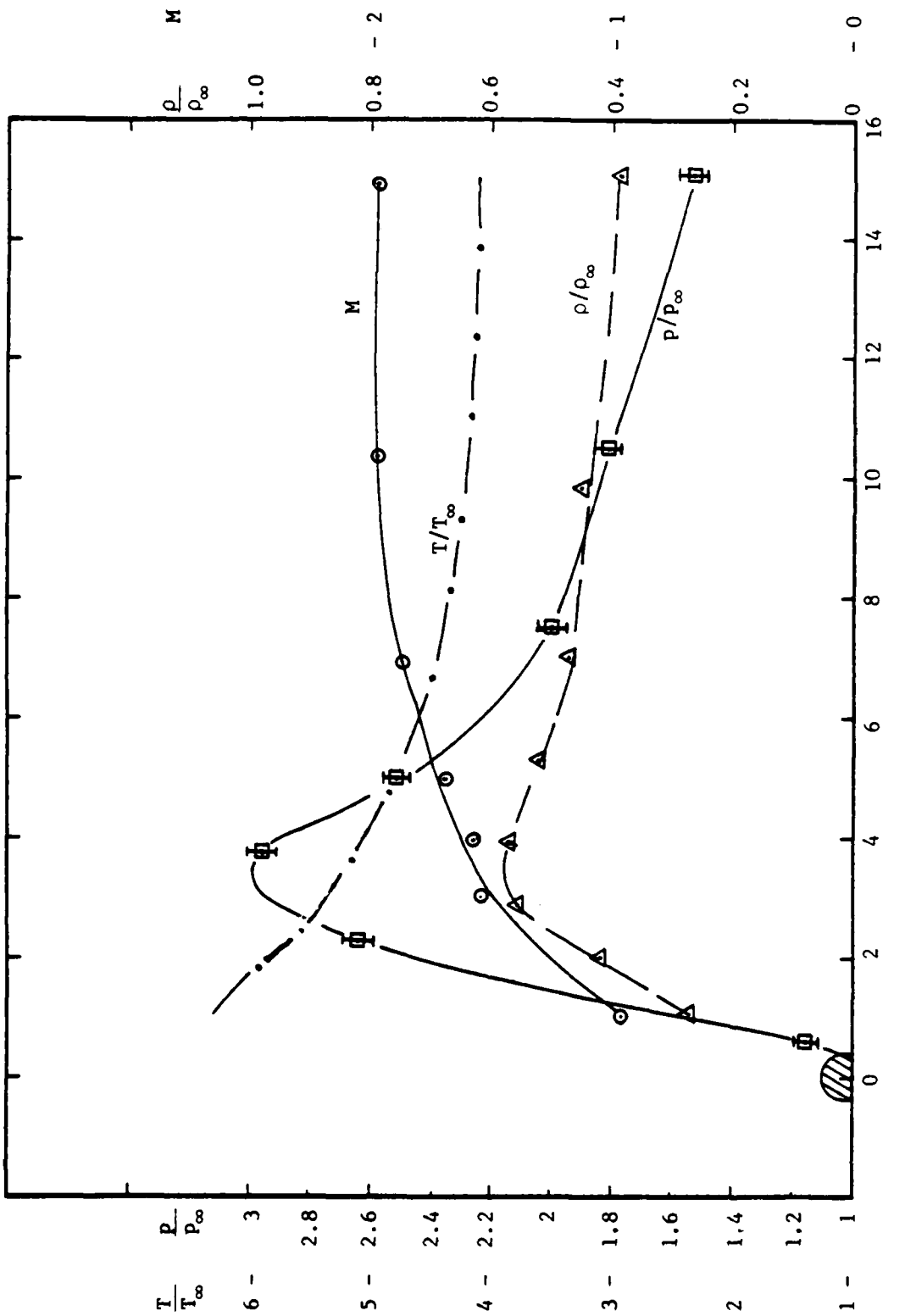

Figure 7. Wake flow variables along center line calculated from data of Ref. (3).

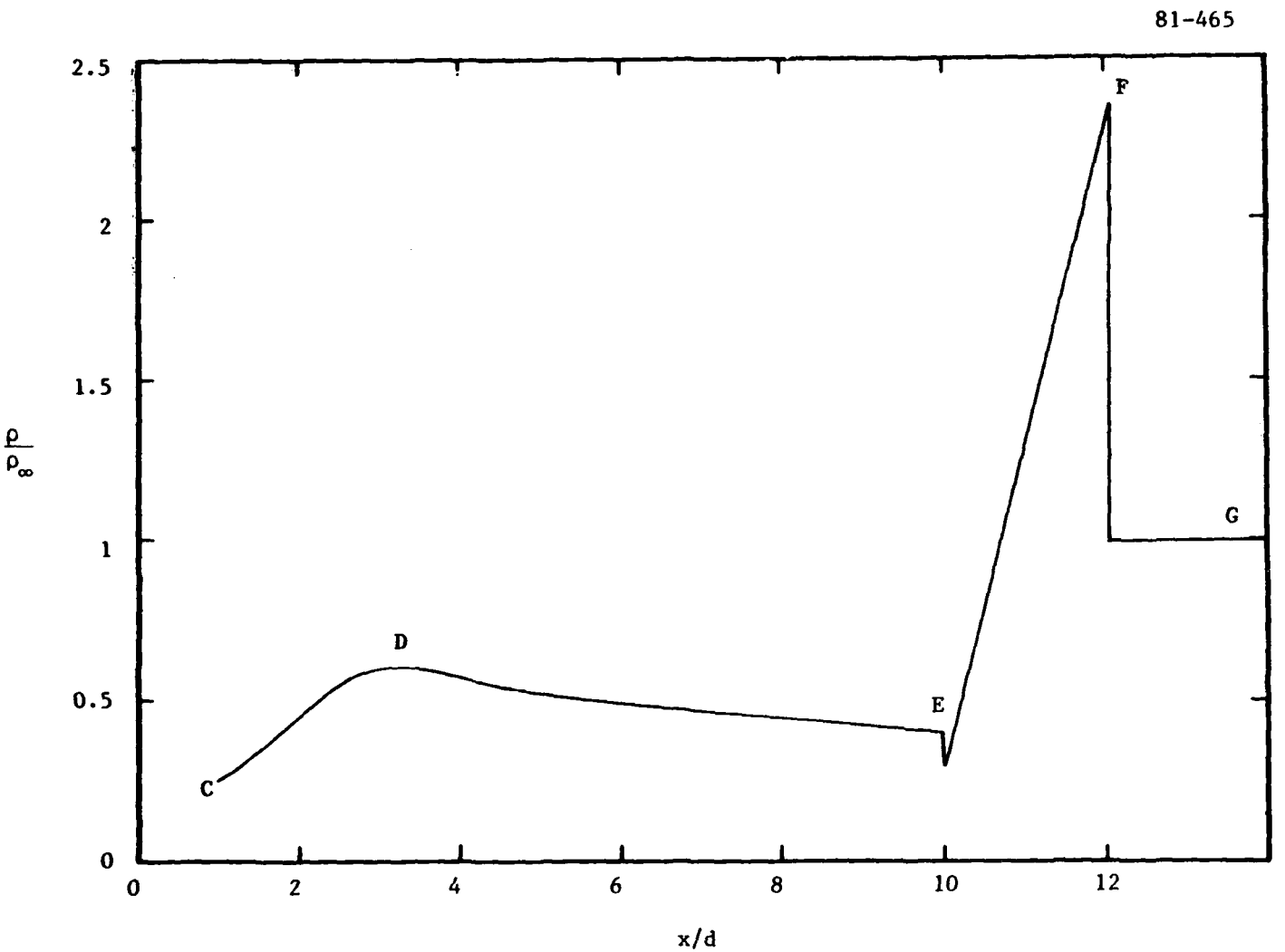

Figure 8. Density ratio as a function of downstream distance.

position along the line of sight, and then to analyse the radiation chemistry according to the local density. The electron energy along the line of sight may be calculated by integrating the electron beam energy loss along the electron streamline. The radiation chemistry calculation is best done in the frame of the vehicle. Then the evolution of species X is governed by

$$\frac{\partial [X]}{\partial t} + \nabla \cdot ([X]\underline{u}) = \frac{\partial [X]}{\partial t}_{\text{chemical}}$$

The vehicle movement is then accounted for by the convection term, and the right hand side represents the chemical generation of X. The diffusion term has been neglected because of the high Reynolds number (~2000) of the flow.

CONCLUSION

The flow field around the EXCEDE vehicle at 80 km altitude has been characterized. There is a bow shock that wraps around the front surface of the vehicle. Behind the vehicle is a wedge-shape recirculation region which terminates in a high compression region termed the neck. The wake shock emerges from the neck and equilibrates the pressure of the overexpanded flow behind the bow shock to that of the wake. The density in the wake is approximately half of that of the freestream while the density at the bow shock is over twice the freestream value. The regions of strong atmospheric emission recorded by the on-board camera are a result of the electron irradiation of the bow shock.

PART 4

LONG LIVED BEAM-INDUCED CHEMILUMINESCENCE IN PRECEDE I EXPERIMENT

Prepared by

Mark S. Zahniser
Aerodyne Research, Inc.
Bedford Research Park
Crosby Drive
Bedford, MA 01730

INTRODUCTION

The visible emissions observed from the ground in the Precede I experiment may be categorized into three types: (1) prompt radiation which occurs during the period of the electron beam, (2) a short lived chemiluminescent wake involving the outgassing products of the rocket motor, and (3) long lived chemiluminescence induced by the electron beam. The first two types of emission are apparent in photographs taken from the ground based tracking cameras which view the rocket trajectory from the side (Denver and Cloudcroft sites) and have been described previously[1,2]. The long lived chemiluminescence is evident in visible photographs[3] from a fixed camera located at the end viewing site (Tiff) which is situated in the plane of the rocket trajectory. This section of the report attempts to analyze this chemiluminescence in terms of molecular species responsible for the emission.

This is a preliminary report on the analysis of the long-lived visible chemiluminescent data. The effort started with placing altitude profiles on the ground based photographs and making frame-to-frame altitude correlations. We then worked with W. Boquist on the regions of the film requiring the absolute light intensities. A search for long-lived visible emitters indicated several possible species which could be produced by electron beam irradiation. The $NO + O \rightarrow NO_2 + h\nu$ air afterglow was chosen for more detailed analysis, since its spectral distribution best matched that of the film. We shall show that theoretical predictions of the NO_2 emission are several orders of magnitude below the observed intensity, concluding that some other species is producing the radiation.

---

[1]R.R. O'Neil, F. Bien, D. Burt, J.A. Sandock, and A.T. Stair, Jr., "Summarized Results of the Artificial Auroral Experiment, Precede," J. Geophys. Res. 83, 3273 (1978).

[2]R.R. O'Neil, E.T.P. Lee, and E.R. Huppi, "Auroral O(^{1}S) Production and Loss Processes: Ground-Based Measurements of the Artificial Auroral Experiments Precede", J. Geophys. Res. 84, 823 (1979).

[3]W.P. Boquist, "Photographic History of AFGL Project Precede I Experiment," Technical Report TIC802, Technology International Corporation, Bedford, Massachusetts (1979).

DESCRIPTION OF THE EXPERIMENTAL DATA

The beam-induced long lived chemiluminescence is shown in Figure 1 where it appears as a series of light and dark spots on the film record due to the 0.5 Hz square wave modulation of the electron beam. The rocket trajectory and camera field of view are shown in Figure 2. The photograph in Figure 1 was recorded with a 4s exposure time. The bright streak towards the bottom of the photograph is due to prompt emission during two beam pulses which are joined by the short lived chemiluminescent wake from rocket motor outgassing. The photograph was taken from 242 to 246s after launch which corresponds to a vehicle altitude of 101 to 99 km.

The long lived chemiluminescence is strongest in the altitude region from 95 to 115 km with a maximum in both intensity and duration at 105 km. The camera continued to operate for 200s after the rocket passed through this altitude region (240 to 440s) after launch with a series of 2s, 4s, and 16s exposures. During this time period the chemiluminescent trail was distorted by wind shear, and the initially discrete pulses were smeared together by diffusion. The trial is clearly apparent, however, in the 16s exposure 200s after the electron beam irradiation as shown in Figure 3.

The photographs were taken with a large aperture f/0.75, 150 mm focal length lens at a slant range of 120 km. The spectral coverage of the Kodak 2485 recording film is from 300 to 700 mm. The spectral sensitivity curve is shown in Figure 4.

The exposure of the film has been estimated from microdensitometer traces by Photometrics, Inc. in conjunction with W.P. Boquist of Technology International Corporation. The bright pulses in Figure 1 have a film exposure of 0.02 ergs cm^{-2} and an area of $5x10^{-4} cm^2$ on the film negative. The background exposure between the pulses and in the starless areas is ~0.01 ergs cm^2.

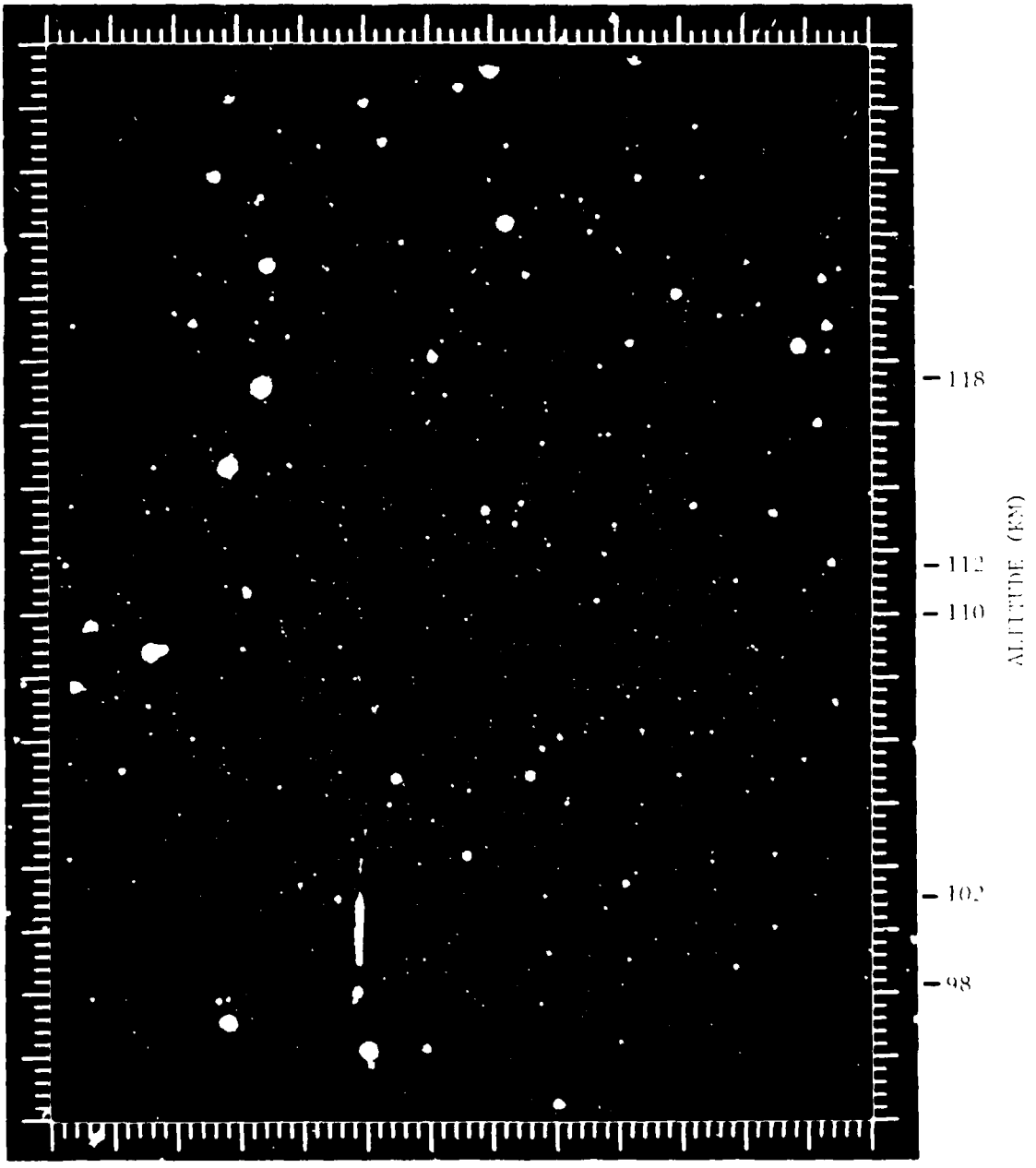

Figure 1. Chemiluminescent trail induced by electron beam. The bright streak at the bottom of the photo is due to prompt emission from the electron beam. Exposure time is 4s starting 24.2s after launch.

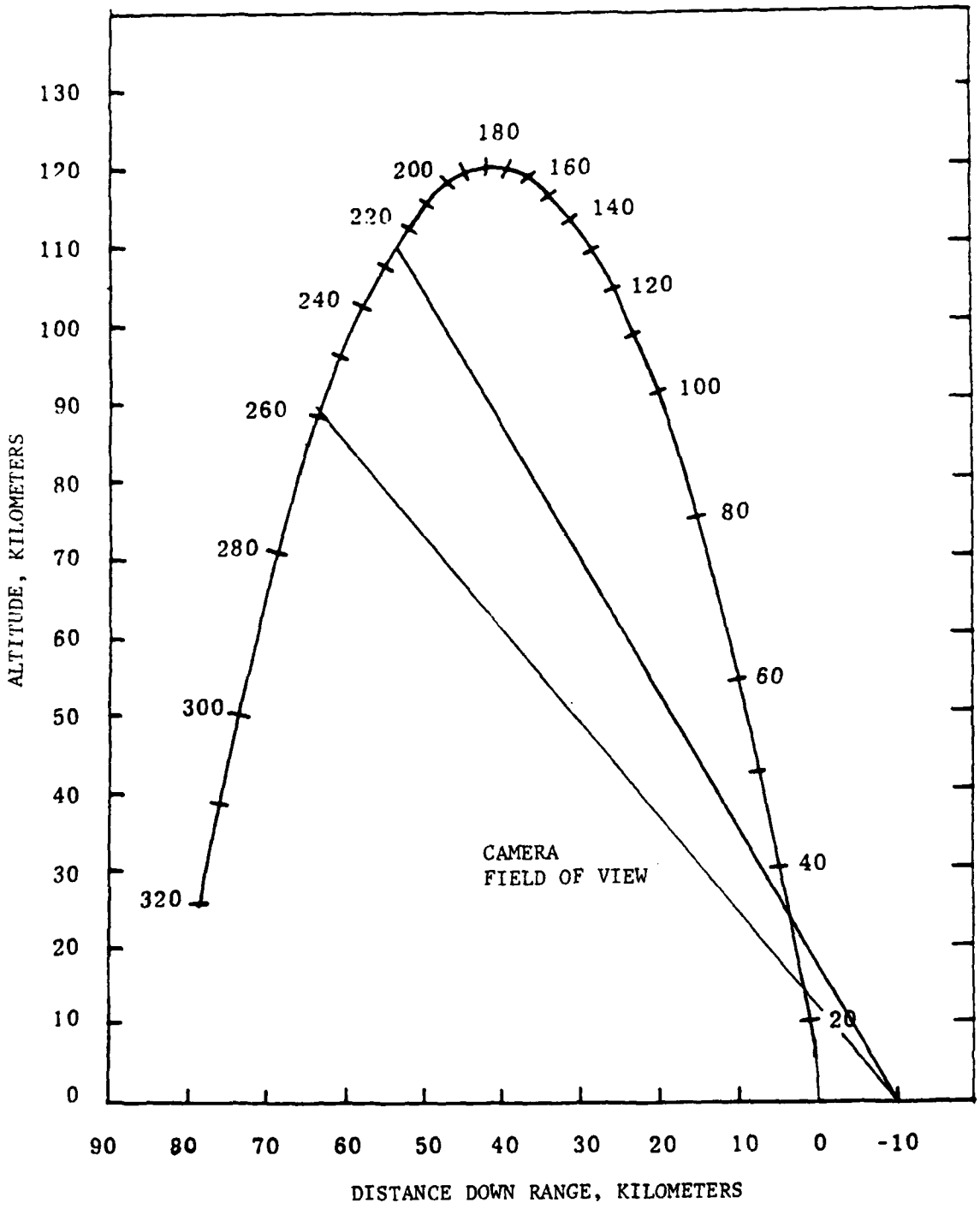

Figure 2. Precede vehicle trajectory showing field of view of camera for photograph in Figure 1. Cross marks on trajectory indicate time after launch in seconds.

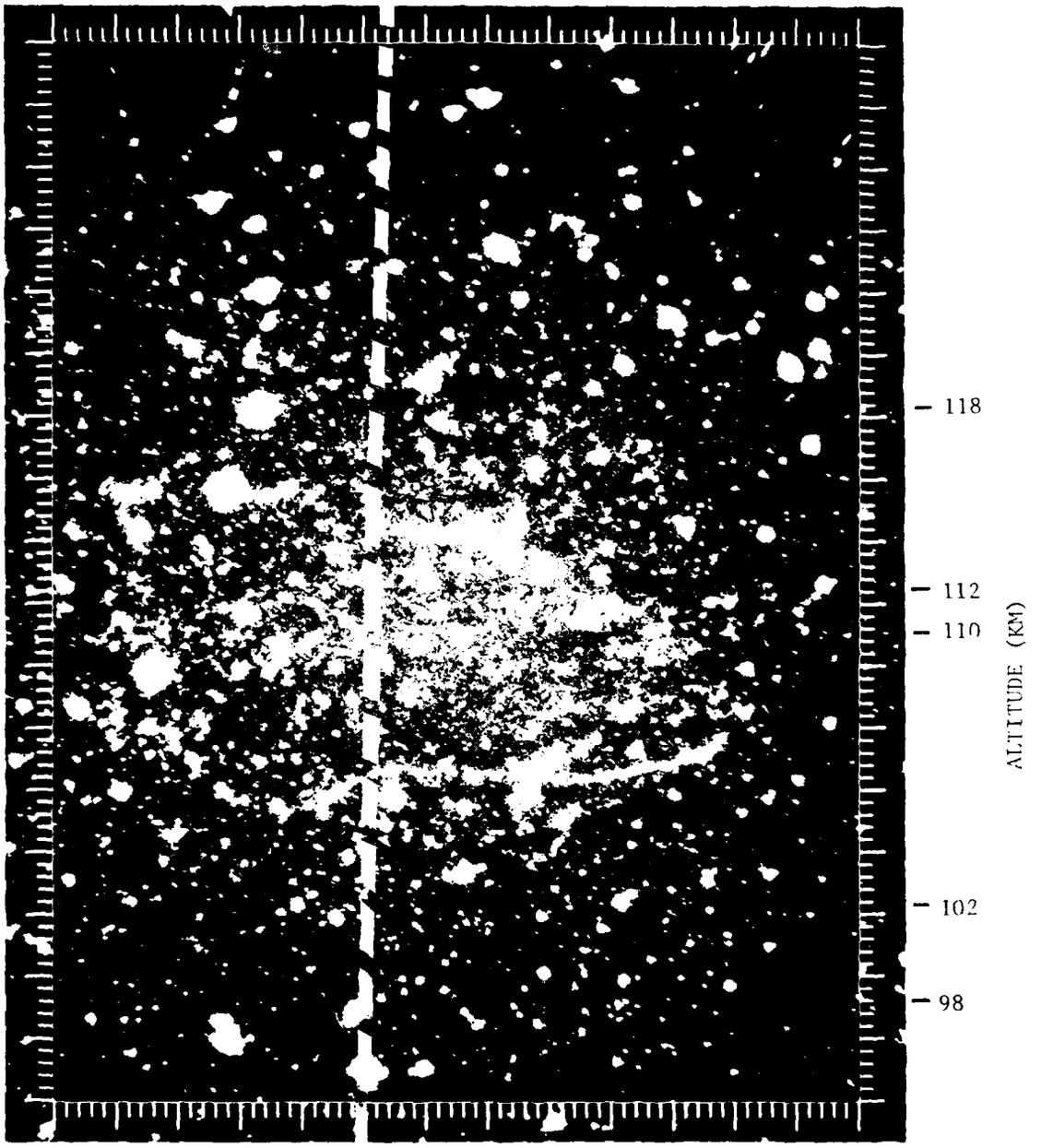

Figure 3. Chemiluminescent trail 200s after irradiation (440s after launch). Trail is displaced by wind shear from its original position as shown by the dashed line. Exposure time is 16s.

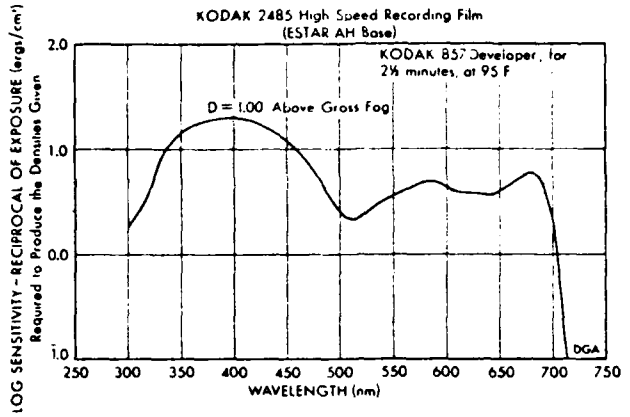

Figure 4. Spectral sensitivity curve for Kodak 2485 film.

The radiance of the object is related to film exposure by

$$R \text{ (ergs cm}^{-2} \text{ s}^{-1} \text{ sr}^{-1}) = \frac{4}{\pi} (f/n)^2 \frac{1}{T_{lens}} \frac{1}{T_{atm}} \frac{1}{t} E \text{ (ergs/cm}^2)$$

where the numerical aperature f/n = 0.75 is the ratio of focal length to diameter of the optics, T_{lens} and T_{atm} are the transmissions of the optics and the atmosphere, and t is the exposure time. Assuming 0.7 for both transmission factors and a 4s exposure time, the radiance is 7×10^{-3} ergs cm^{-2} s^{-1} sr^{-1}. The column photon emission rate may be obtained by

$$I = R \, 4\pi \, \lambda/hc \text{ (photons cm}^{-2} \text{ s}^{-1})$$

where λ is the photon wavelength, h is Plank's constant, and c is the velocity of light. For 600 nm photons the emission rate corresponding to the observed radiance is 2.8×10^{10} photons $cm^{-2}s^{-1}$ or 28 k Rayleighs.

The background intensity on the film of 0.01 ergs cm^{-2} similarly corresponds to a column emission rate of ~10 kR. This background may be attributed to starlight scattered by the earth's atmosphere. Typical values for a clear night sky are on the order of 1-2 Rayleighs/Å which gives a total of 4 to 8 kR integrated over the 3000 Å to 7000 Å film response. After subtracting this background, the column intensity due to the beam induced chemiluminescence in Figure 1 is on the order of 10 to 20 kR.

The photon flux may be integrated over an individual pulse to give the total emission rate from the electron beam irradiated volume. The pulse image on the film negative is rectangular in shape with dimensions 0.035 by 0.015 cm measured as a full width at half the maximum density. The microdensitometer record has an approximately Gausian density contour across the width of the pulse with a maximum density of 0.02 ergs cm^{-2} and a background density of 0.01 ergs cm^{-2}. Thus the integrated density over the entire pulse is 5×10^{-6} ergs corresponding to 1.5×10^{6} photons (λ = 6000 Å). The collection efficiency for the optical system is

$$\varepsilon = \frac{1}{16} \left(\frac{1}{f/n}\right)^2 \left(\frac{F}{r}\right)^2 T_{atm} \; T_{lens}$$

$$= 1 \times 10^{-13}$$

where F is the lens focal length (15 cm) and r is the range (120 km). This gives a volume emission of 1.5×10^{19} photons during the 4s exposure or a volume emission rate of 4×10^{18} photons s^{-1}.

ANALYSIS OF POSSIBLE EMITTERS

The requirements for the emission lifetime, τ, and the emitting species concentration, n, may be estimated by determining the volume irradiated by the

electron beam. The penetration of the electron beam at 105 km altitude is 600m with a beam diameter of 20m.[1] The vehicle velocity is 600m s^{-1} and is traveling nearly perpendicular to the earth's magnetic field at this point in the trajectory. This gives an irradiated volume during a 1s pulse of 600m x 600m x 20m = 7.2 x 10^{12} cm^3.

The ratio of emitter concentration, n, to emission lifetime, τ, may be obtained by combining the volume emission rate, R, and the irradiated volume, V:

$$n/\tau = R/V$$

$$= 5 \times 10^{5} \text{ cm}^{-3} \text{ s}^{-1}$$

The lifetime observed from the photographic record of ~100s is a combination of radiative decay, quenching, and chemical reaction of the emitting species. If the dominant process were radiative decay, this would imply an emitter concentration $n \geq 5 \times 10^{7}$ cm^{-3} to account for the observed intensity. If quenching or chemical reaction is responsible for the observed lifetime, a larger emitter concentration is required.

THE AIR AFTERGLOW ($NO + O \rightarrow NO_2^* \rightarrow NO_2 + h\nu$)

The reaction between nitric oxide formed in the beam and ambient atomic oxygen was considered as a source candidate. This well studied emission system radiates throughout the visible and into the infrared from 400 to 2000 nm with a maximum at 600 nm. The lifetime is determined by the ambient pressure, temperature, and atomic oxygen concentration. It has been used for measuring O-atom concentrations in the 80 - 140 km region from rocket-borne NO releases,[4] and has also been used extensively in laboratory studies of O-atom reactions.[5]

[4]E. Van Hemelrijck, "Atomic Oxygen Determination From a Nitric Oxide Point Release in the Equational Lower Thermosphere," J. Atm. and Terres. Phys. 43, 345 (1981).

[5]F. Kaufman, "The Air Afterglow Revisited," in Chemiluminescence and Bioluminescence, edited by M.J. Cormier, D.M. Hercules, and J. Lee (Plenum, New York) (1973), pp. 83-101.

The radiative mechanism is a combination of two body and three body collision processes which may be most simply described by the reactions:

$$NO + O \rightarrow NO_2 + h\nu \qquad 1$$

$$NO + O + M \rightarrow NO_2^* + M \qquad 2$$

$$NO_2^* + M \rightarrow NO_2 + M \qquad 3$$

$$NO_2^* \rightarrow NO_2 + h\nu \qquad 4$$

This yields the rate constant expression:

$$k_r(M) = k_1 + \frac{k_2\, k_4\, [M]}{k_4 + k_3\, [M]}$$

which varies with pressure from $k_r(o) = k_1$ in the low pressure limit to $k_r(\infty) = k_1 + (k_2\, k_4/k_3)$ in the high pressure limit. The change-over occurs in the 10^{-3} to 1 torr pressure region with the ratio $k_r(\infty)/k_r(o)$ ~15 at 300K.[6] There is a spectral dependence to this fall-off ratio which increases from unity at the short wavelength threshold near 397 nm to a value of ~10 at 600 nm. Combining the measurements of $k_r(\infty) = 3.7 \times 10^{-17}$ photons cm^3 s^{-1} at 300K by Golomb and Brown[7] over the spectral range 400-800 nm with an average fall-off ratio $k_r(\infty)/k_r(o)$ ~8 for this spectral region gives a value for $k_r(o)$ ~5×10^{-18} photons cm^3 s^{-1} for the two body rate constant appropriate for the 105 km altitude region where the pressure is ~10^{-4} torr and the reaction is in its low pressure limit.

---

[6] K.H. Becker, W. Groth, and D. Thran, "Mechanism of the Air Afterglow NO + O → NO_2 + hν," XIVth Combustion Symposium (The Combustion Institute, Pittsburgh, PA) (1972), pp. 353-363.

[7] D.Golomb and J.H. Brown, "The Temperature Dependence of the NO + O Chemiluminous Recombination," J. Chem. Phys. 63, 5246 (1975).

Nitric oxide is produced by the reactions

$$N(^2D) + O_2 \rightarrow NO + O \qquad 5$$

$$N_2 (A\ ^3\Sigma_u^+) + O \rightarrow NO + N(^2D) \qquad 6a$$
$$\rightarrow N_2 + O(^1S) \qquad 6b$$

where $N(^2D)$ and $N_2(A)$ are formed by electron impact in the reactions

$$N_2 + e \rightarrow 0.5\ N(^2D) + 0.5\ N(^4S) + N^+ + 2e \qquad 7$$
$$N_2 + e \rightarrow N_2^+ + e \qquad 8$$
$$N_2^+ + e \rightarrow N(^2D) + N(^4S) + e \qquad 9$$
$$N_2 + e \rightarrow N_2(A) \qquad 10$$
$$N_2 + e \rightarrow N_2(B\ ^3\Pi_g) \qquad 11$$
$$N_2(B) \rightarrow N_2(A) + h\nu \qquad 12$$

Production via reaction 5 is predominate with current estimates of $N(^2D)$ formed in the 3 kV electron beam on the order of 2 $N(^2D)$ per ion pair compared to 0.5 $N_2(A)$ per ion pair. The branching ratio of 0.5 for each channel of reaction 6 further reduces the importance of $N_2(A)$ compared to $N(^2D)$ in NO production.

The amount of NO produced by the beam may be estimated by assuming an upper limit of 2 $N(^2D)$/ion pair all of which form NO. The number of ion pairs formed per pulse is obtained by assuming an energy deposition rate of 35 eV/ion pair. This gives an ion pair production rate of 3.5×10^{20} ion pairs/pulse for the 2.5 kV, 0.8 A, 1s, beam which corresponds to a maximum NO production of 7×10^{20} NO/pulse. For an irradiated volume at 105 km altitude of 7×10^{12} cm^3 this yields an NO concentration of 1×10^8 cm^{-3}. This simple estimate is similar to that obtained from a more complete model for $O(^1S)$ emission from Precede[2] which gives a maximum NO concentration of 3×10^8 cm^{-3}.

The photon emission rate for the air afterglow is then

$$I = k_r [O] [NO]$$

$$= (5 \times 10^{-18} \text{ cm}^3 \text{ s}^{-1}) \ (5 \times 10^{11} \text{ cm}^{-3}) \cdot (1 \times 10^{8} \text{ cm}^{-3})$$

$$= 250 \text{ photons cm}^{-3} \text{s}^{-1}$$

where the atomic oxygen density is taken as the average value of several measurements at 105 km by Dickenson et al.[8] This corresponds to a column emission rate over the 600m irradiated depth of 15 Rayleighs, or a total volume emission rate of 1.8×10^{15} photons/pulse.

The calculated emission rates are three orders of magnitude smaller than the observed values for both column emission and integrated volume emission. Although the calculated intensity could be increased if one considered additional atomic oxygen formed by the electron beam, the discrepancy is still too large to attribute the chemiluminescence to the $O + NO \rightarrow NO_2 + h\nu$ mechanism.

CONCLUSIONS

Ground based photographic records of the Precede I experiment show a long lived visible chemiluminescent trail with a lifetime on the order of 10 to 100s. The trail exists initially as discrete pulses and is therefore attributed to a species formed by the electron beam rather than from outgassing from the launch vehicle. Although the air afterglow system $NO + O \rightarrow NO_2^* \rightarrow NO_2 + h\nu$ has a suitable spectral distribution and lifetime for the emission, the amount of NO produced by the electron beam is insufficient to account for the observed intensity. There are several other possible emitting

[8] P.H.G. Dickinson, W.C. Bain, L. Thomas, E.R. Williams, D.B. Jenkins, and N.D. Twiddy, "The Determination of the Atomic Oxygen Concentration and Associated Parameters In the Lower Ionosphere," Proc. Roy. Soc. Lond. A 369, 379,(1980).

species which could be responsible for the observed chemiluminescence. Excited molecular oxygen states $O_2(c\ ^1\Sigma_u^-)$ and $(A'\ ^3\Delta_u)$ have radiative lifetimes of 25 - 50s and 12s, respectively, and are produced by electron beam irradiation. These species radiate throughout the 400 - 700 nm region of the film response curve and should receive further consideration as producers of the chemiluminescence.


ATE
LME